nature neuroscience

ARTICLES

https://doi.org/10.1038/s41593-022-01063-z

Check for updates

Meningeal lymphatic vessels mediate neurotropic viral drainage from the central nervous system

Xiaojing Li[1,2,3,4,10], Linlin Qi[1,2,4,10], Dan Yang[2,4], ShuJie Hao[1,2], Fang Zhang[2,3,4], Xingguo Zhu[1,2], Yue Sun[5], Chen Chen[6], Jing Ye[6], Jing Yang[5], Ling Zhao[6], Daniel M. Altmann[7], Shengbo Cao[6], Hongyan Wang[8,9] ✉ and Bin Wei[1,2,3,4] ✉

Recent studies have demonstrated that brain meningeal lymphatic vessels (MLVs) act as a drainage path directly into the cervical lymph nodes (CLNs) for macromolecules contained in the cerebrospinal fluid (CSF). However, the role of MLVs during CNS viral infection remains unexplored. Here, we found that infection with several neurotropic viruses in mice promotes MLV expansion but also causes impaired MLV-mediated drainage of macromolecules. Notably, MLVs could drain virus from the CNS to CLNs. Surgical ligation of the lymph vessels or photodynamic ablation of dorsal MLVs increased neurological damage and mortality of virus-infected mice. By contrast, pretreatment with vascular endothelial growth factor C promoted expansion of functional MLVs and alleviated the effects of viral infection. Together, these data indicate that functional MLVs facilitate virus clearance, and MLVs represent a critical path for virus spreading from the CNS to the CLNs. MLV-based therapeutic strategies may thus be useful for alleviating infection-induced neurological damage.

The CNS is physically protected by bony structures and is also enveloped by the meninges and surrounded by the cerebrospinal fluid (CSF). Recent studies have shown that meningeal lymphatic vessels (MLVs) are located both dorsally and basally beneath the skull[1,2]. Like conventional lymphatic endothelial cells (LECs), meningeal LECs (mLECs) express multiple markers, such as CD31, vascular endothelial growth factor receptor 3 (VEGFR-3), prospero homeobox protein 1 (PROX1), podoplanin (PDPN) and lymphatic vessel endothelial hyaluronan receptor 1 (LYVE-1)[2,3]. Emerging evidence has shown that MLVs are able to carry CSF components and immune cells from the CNS to the cervical lymph nodes (CLNs) in the brain[1,2,4,5]. Recent reports have suggested that MLVs are involved in the pathological processes of multiple neurologic diseases. Disruption of MLVs aggravates parenchymal amyloid-β accumulation in Alzheimer's disease pathology[6] and also significantly reduces the efficacy of combined anti-PD-1/CTLA-4 checkpoint therapy in brain tumor models[7,8]. However, ablation of MLVs could limit antigen transport and T cell migration, resulting in reduced severity of multiple sclerosis[4,9]. Despite these valuble findings, changes in MLVs and their roles during neurotropic virus infection remain uncharacterized. A range of viruses, including Zika virus (ZIKV), Japanese encephalitis virus (JEV), rabies virus (RABV), herpes simplex virus 1 (HSV-1) and vesicular stomatitis virus (VSV), can invade the CNS and cause acute inflammation of the brain parenchyma, usually accompanied by meningitis and neurologic symptoms[10–13].

The brain is well protected against microbial invasion by the blood–brain barrier (BBB) and the blood–CSF barrier, and many studies of viral dissemination focus on movement across tissue–brain barriers[14,15]. In addition, the olfactory and trigeminal nerves represent pathways by which viruses enter the brain without encountering the BBB or the blood–CSF barrier[13]. These nerves are well recognized as portals of entry for many viruses. However, other possible mechanisms for virus dissemination inside or outside of the CNS are less clear. Because the 'meningeal lymphatic' system in the brain, including MLVs, has the capacity for carrying CSF components and immune cells from the CNS to the peripheral CLNs, it is interesting to ask whether the lymphatic system is able to support viral spread from the CNS to the periphery.

To investigate the pathological response of MLVs following neurotropic viral infection, we used various mouse models infected with RABV, ZIKV, HSV-1, JEV and VSV. We demonstrated that specific photodynamic ablation of dorsal MLVs or ligation of the deep CLNs (dCLNs) significantly exacerbated neurological damage and mortality during JEV infection. VEGF-C pretreatment caused expansion of functional MLVs and alleviated CNS damage and mortality of virus-infected mice. By contrast, viral infection promoted MLV expansion with partial impaired function, showing slower dissemination and clearance of viruses in the CNS.

Results

Viral CNS infections induce meningeal lymphangiogenesis. To determine whether neurotropic virus infection is capable of inducing meningeal lymphangiogenesis in the CNS, 5-week-old C57BL/6 mice were intravenously infected with JEV to induce severe viral

[1]Institute of Geriatrics, Affiliated Nantong Hospital of Shanghai University (The Sixth People's Hospital of Nantong), School of Medicine, Shanghai University, Nantong, China. [2]Shanghai Engineering Research Center of Organ Repair, School of Life Sciences, Shanghai University, Shanghai, China. [3]Cancer Center, Shanghai Tenth People's Hospital, School of Medicine, Tongji University, Shanghai, China. [4]State Key Laboratory of Virology, Wuhan Institute of Virology, Chinese Academy of Sciences, University of Chinese Academy of Sciences, Wuhan, China. [5]School of Life Sciences, Peking University, Beijing, China. [6]State Key Laboratory of Agricultural Microbiology, Huazhong Agricultural University, Wuhan, China. [7]Department of Immunology and Inflammation, Imperial College, Faculty of Medicine, Hammersmith Hospital, London, UK. [8]State Key Laboratory of Cell Biology, Shanghai Institute of Biochemistry and Cell Biology, Center for Excellence in Molecular Cell Science, Chinese Academy of Sciences, University of Chinese Academy of Sciences, Shanghai, China. [9]School of Life Science, Hangzhou Institute for Advanced Study, University of Chinese Academy of Sciences, Hangzhou, China. [10]These authors contributed equally: Xiaojing Li, Linlin Qi. These authors jointly supervised this work: Hongyan Wang, Bin Wei. ✉e-mail: hongyanwang@sibcb.ac.cn; weibinwhy@shu.edu.cn

encephalitis. We investigated changes in MLVs by immunostaining with antibodies recognizing LYVE-1, VEGFR-3 and PDPN, classical markers of LECs. Expansions of LYVE-1$^+$, VEGFR-3$^+$ or PDPN$^+$ vessels in the confluence of sinuses (COS) of the meninges and LYVE-1$^+$ vessel area in the transverse sinuses (TS) of the meninges were observed, along with increased diameter of LYVE-1$^+$ vessels around the superior sagittal sinus (SSS) in JEV-infected mice (Fig. 1a,b and Extended Data Fig. 1a,b). The enlarged LYVE-1$^+$ vessel area along the COS also occurred in mice intracranially injected with JEV (Extended Data Fig. 1c). Expression of VEGF-C and inflammatory cytokines, such as interleukin-6 (IL-6) and tumor necrosis factor-α (TNFα), was enhanced at 7 d in the brain of JEV-infected mice (Fig. 1c and Extended Data Fig. 1d). Meanwhile, viral loads in the brain and the disease severity of infected mice (recorded as various behavior scores) increased at days 3–4 and peaked at days 6–7 after infection (Extended Data Fig. 1e). The increase in LYVE-1$^+$ vessel area around the COS and TS appeared 3 d after JEV infection (Extended Data Fig. 1f).

To investigate whether other viral infections in the brain also induce meningeal lymphangiogenesis, C57BL/6 mice were infected by intranasal injection of VSV. We observed virus in the CNS and reduction in body weight (Extended Data Fig. 1g,h). Consistent with the observations in JEV-infected mice, the expansion of dorsal MLVs along the COS and TS in the meninges was also shown in VSV-infected mice by analysis of LYVE-1$^+$, VEGFR-3$^+$ or PDPN$^+$ vessel area (Fig. 1d,e and Extended Data Fig. 1i). The expression levels of VEGF-C and *Il6*, *Tnfa* and *Ccl5* in the brain were enhanced following VSV infection in the CNS (Fig. 1f and Extended Data Fig. 1h). Following corneal infection with HSV-1, we observed viral invasion of the mouse brain and reduced body weight (Extended Data Fig. 2a). Similarly, the area of LYVE-1$^+$ vessels and the diameter of the vessels were also increased in the meninges of HSV-1-infected mice (Fig. 1g and Extended Data Fig. 2b), which was accompanied with increased expression of VEGF-C, *Tnfa* and *Ccl5* in brain (Fig. 1h and Extended Data Fig. 2c).

In terms of high case fatality rates and poor therapeutic efficacy of treatments, RABV and ZIKV are a global threat to public health. We next infected C57BL/6 mice by the intramuscular route with RABV (CVS-B2c strain, dose lethal to 50% of animals tested (LD_{50}) of 100)[16], and severely infected mice showing paralysis at 8 d postinfection (d.p.i.) were used to investigate changes in MLVs. We observed increased LYVE-1$^+$ vessel area in the COS of meninges (Fig. 1i) and abundant protruding capillary branches with blunt ends in dorsal MLVs running along the COS and TS (Fig. 1j and Extended Data Fig. 2d,e). In addition, ZIKV was intraperitoneally injected into AG6 (interferon (IFN) receptor-deficient) mice as previously reported[17]. We confirmed substantial virus in the CNS and reduced body weight (Extended Data Fig. 2g,h) and expanded LYVE-1$^+$ vessels along the sinuses in the meninges, especially around the COS and TS (Fig. 1l and Extended Data Fig. 2i). Notably, expression of VEGF-C and *Il1b*, *Il6*, *Il10*, *Ccl5* and *Tnfa* in the brains of RABV- or ZIKV-infected mice were significantly increased compared to the control mice (Fig. 1k,m and Extended Data Fig. 2f,j), Collectively, these data indicate that JEV, VSV, HSV-1, RABV or ZIKV infection could induce lymphangiogenesis of dorsal MLVs in the CNS of mice.

Basal MLVs were reported by recent studies[1,8]. We next asked whether the changes in basal MLVs following neurotropic viral infection and lymphangiogenesis of basal MLVs were also observed in JEV- or RABV-infected mouse brains (Extended Data Fig. 2k). Consistent with our observation on the expansion of both basal and dorsal MLVs, LECs (CD31$^+$PDPN$^+$ cells) from isolated meninges were enhanced following JEV infection, offering direct evidence to support lymphangiogenesis of MLVs (Fig. 1n). Importantly, expression levels of PDPN were substantially enhanced in the meninges of JEV-infected mice compared to controls (Fig. 1o). To further confirm this, human LECs (hLECs) were treated in vitro with JEV or inactivated JEV or were left untreated, followed by analysis of the expression of *PDPN* and other proliferation-associated genes, including *FOS*, *JUN* and *BCL2*. Consistently, JEV-infected hLECs showed increased expression of *PDPN* and *FOS*, *JUN* and *BCL2* (Extended Data Fig. 2l). Together, our observations indicate that viral CNS infection could promote expansion of MLVs.

Three-dimensional (3D) imaging of meningeal lymphangiogenesis after viral infection. Next, 3D imaging analysis was used to observe the detailed stereoscopic morphology on the lymphatic vessels, which showed that the volume of LYVE-1$^+$ vessels was significantly increased in JEV-infected mice (Fig. 2a,b and Supplementary Video 1). To detect dorsal MLVs of the whole meninges dissected from the skull, we performed fluorescence imaging that clearly showed the growth and expansion of LYVE-1$^+$ vessels on whole-mount meninges in RABV- or JEV-infected mice (Fig. 2c,d).

It is critical to record the morphology of local lymphatic vessels in meninges, including those still attached to the skull cap. We therefore used advanced volume fluorescence imaging based on the reported immunolabeling-enabled 3D imaging of solvent-cleared organs plus (iDISCO$^+$) method[18], which was recently used for 3D imaging of nerve fibers[19,20]. The whole skull became near transparent after being processed by the optical-clearing procedure (Fig. 2e) and was immunostained with anti-VEGFR-3. Three-dimensional reconstruction of orthotopic lymphatic vessels is shown in Supplementary Video 2, and representative images showed significantly expanded VEGFR-3$^+$ vessels with increased density in the meninges of JEV-infected mice compared to control mice (Fig. 2f). Together, 3D imaging results confirm that viral CNS infection indeed promotes meningeal lymphangiogenesis.

In addition, we found that the expression of VEGF-C was significantly increased in the brains of virus-infected mice (Fig. 1). To identify the cellular sources of VEGF-C, we immunolabeled brain sections of JEV-infected or uninfected mice with antibodies against neuronal nuclei (NeuN), glial fibrillary acidic protein (GFAP), VEGF-C, JEV E protein and DAPI. After JEV infection, NeuN$^+$ neurons (white arrowheads) and GFAP$^+$ astrocytes (orange arrowheads) produced VEGF-C (Fig. 2g). In addition, Ly6c$^+$CD11b$^+$ monocytes/macrophages in the brains of JEV-infected mice produced VEGF-C (Fig. 2h). These data suggest that neurons, astrocytes and Ly6c$^+$CD11b$^+$ monocytes/macrophages secrete VEGF-C, which then promotes VEGFR-3-dependent lymphangiogenesis in the brain during viral CNS infection.

Impaired MLV drainage function following viral CNS infection. Because viral CNS infection promoted MLV expansion, we next checked whether these newly formed MLVs were functional. The soluble radioactive tracer Evans Blue (EB), was injected in the intracisterna magna (i.c.m.) of mice with or without JEV infection, and the presence of EB in dCLNs was examined over a 1-h period. Shortly after injection (5 min after injection), EB was detected in the control group but was hardly detected in JEV-infected mice (Fig. 3a). At 15 min or 30 min after injection, the increased amount of EB was detected in dCLNs of control mice but was only marginally detected in JEV-infected mice (Fig. 3a). These observations demonstrate that the ability of MLVs to drain constituents into CLNs was impaired in JEV-infected mice.

To further evaluate the ability of MLVs to drain biological molecules, we performed in vivo real-time fluorescence optical imaging to monitor the kinetic biodistribution of Alexa Fluor 647-conjugated ovalbumin (OVA-647) via i.c.m. administration into JEV-infected mice with severe scores. Images were captured from the ventral view of mice at various time points up to 2 h after administration. Shortly after i.c.m. administration of OVA-647, fluorescent signals could be detected at the cervical regions of control mice (30 min; Fig. 3b), but

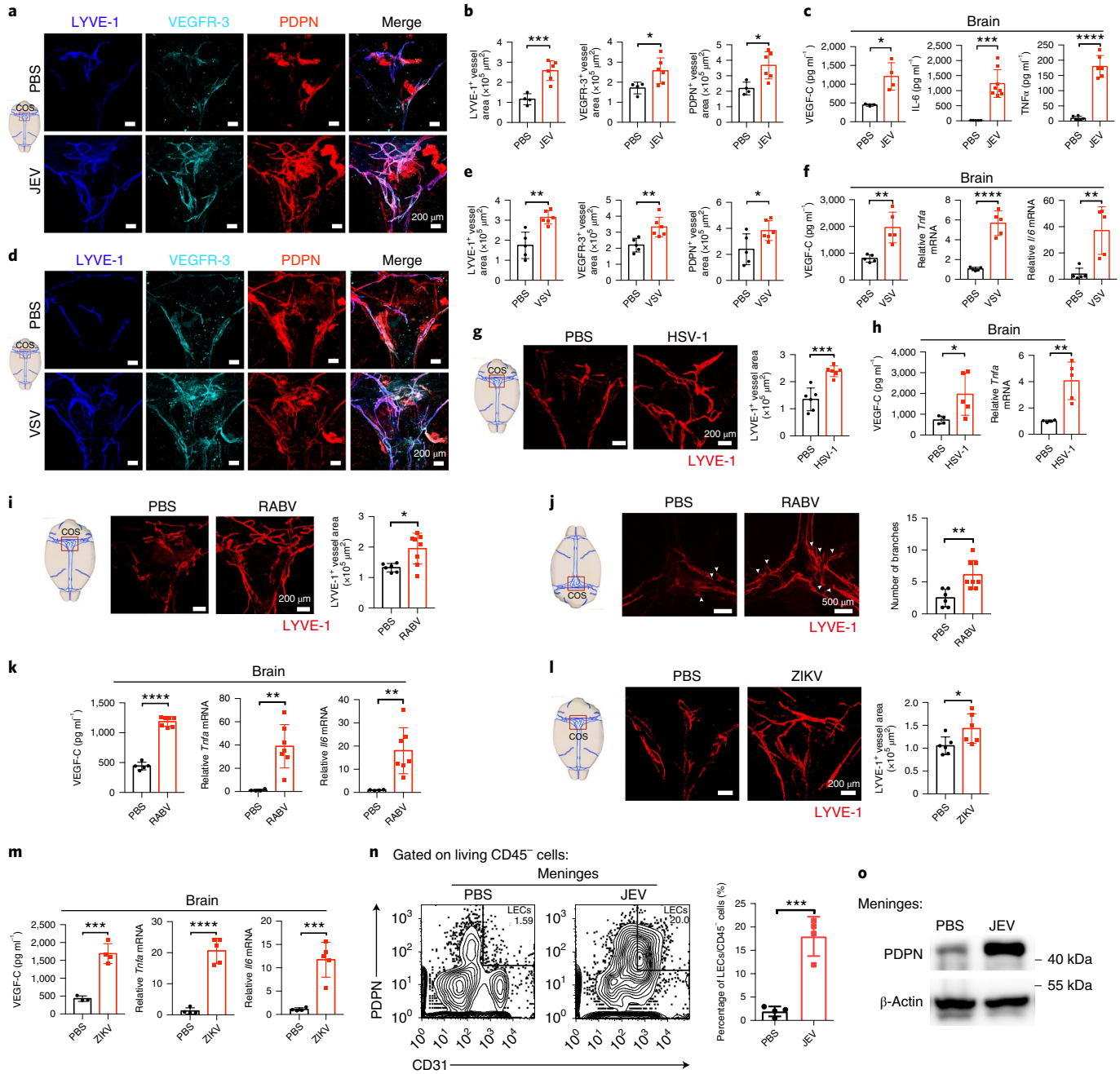

Fig. 1 | Viral CNS infections induce dorsal meningeal lymphangiogenesis. a–c, C57BL/6 mice were intravenously infected with JEV. Representative meningeal LYVE-1, VEGFR-3 and PDPN staining (**a**) and quantification (**b**) at 7 d.p.i. are shown ($n=4$ PBS; $n=6$ JEV). Expression of VEGF-C, TNFα and IL-6 in the brain (**c**) is also shown ($n=3$ or 6 PBS; $n=4$, 6 or 8 JEV). **d–f**, C57BL/6 mice were intranasally injected with VSV. Representative meningeal LYVE-1, VEGFR-3 and PDPN staining (**d**) and quantification (**e**) at 8 d.p.i. (COS) are shown ($n=5$ PBS; $n=6$ VSV). Expression of VEGF-C and mRNA levels of *Tnfa* and *Il6* in the brain (**f**) are also shown ($n=5$). **g**,**h**, C57BL/6 mice were corneally infected with HSV-1. Representative meningeal LYVE-1 staining and quantification at 8 d.p.i. (**g**; COS; $n=6$) and expression of VEGF-C and mRNA levels of *Tnfa* in the brain (**h**; $n=4$ PBS; $n=5$ HSV-1) are shown. **i–k**, C57BL/6 mice were intramuscularly infected with RABV. Representative meningeal LYVE-1 staining and quantification at 8 d.p.i. (COS) (**i**; $n=6$ PBS; $n=8$ RABV), representative meningeal LYVE-1 staining and quantification of lymphatic branches (white arrowheads) at 8 d.p.i. (COS) (**j**; $n=6$ PBS; $n=8$ RABV) and VEGF-C concentrations ($n=5$ PBS; $n=7$ RABV) and mRNA levels of *Tnfa* and *Il6* ($n=4$ PBS; $n=7$ RABV) in the brain (**k**) are shown. **l**,**m**, IFN receptor-knockout (AG6) mice were intraperitoneally injected with ZIKV. Representative meningeal LYVE-1 staining and quantification at 8 d.p.i. (COS) (**l**; $n=6$) and VEGF-C concentrations ($n=3$ PBS; $n=4$ ZIKV) and mRNA levels of *Tnfa* and *Il6* ($n=4$ PBS; $n=5$ ZIKV) in the brain (**m**) are shown. **n**,**o**, The meninges were isolated from JEV-infected mice for FACS analysis. The percentage of LECs ($CD45^-CD31^+PDPN^+$LECs) (**n**) and immunoblot analysis of PDPN (**o**) at 6 d.p.i. are shown. Data are presented as mean ± s.d. Data from at least three independent experiments were obtained with similar results; $^*P<0.05$, $^{**}P<0.01$, $^{***}P<0.001$ and $^{****}P<0.0001$ using a two-tailed, unpaired Student's *t*-test (**b**,**c**,**e**,**f**,**g** (right), **h**,**i** (right),**j** (right), **k**,**l** (right), **m** and **n** (right)). Detailed statistical information is shown in Supplementary Table 2.

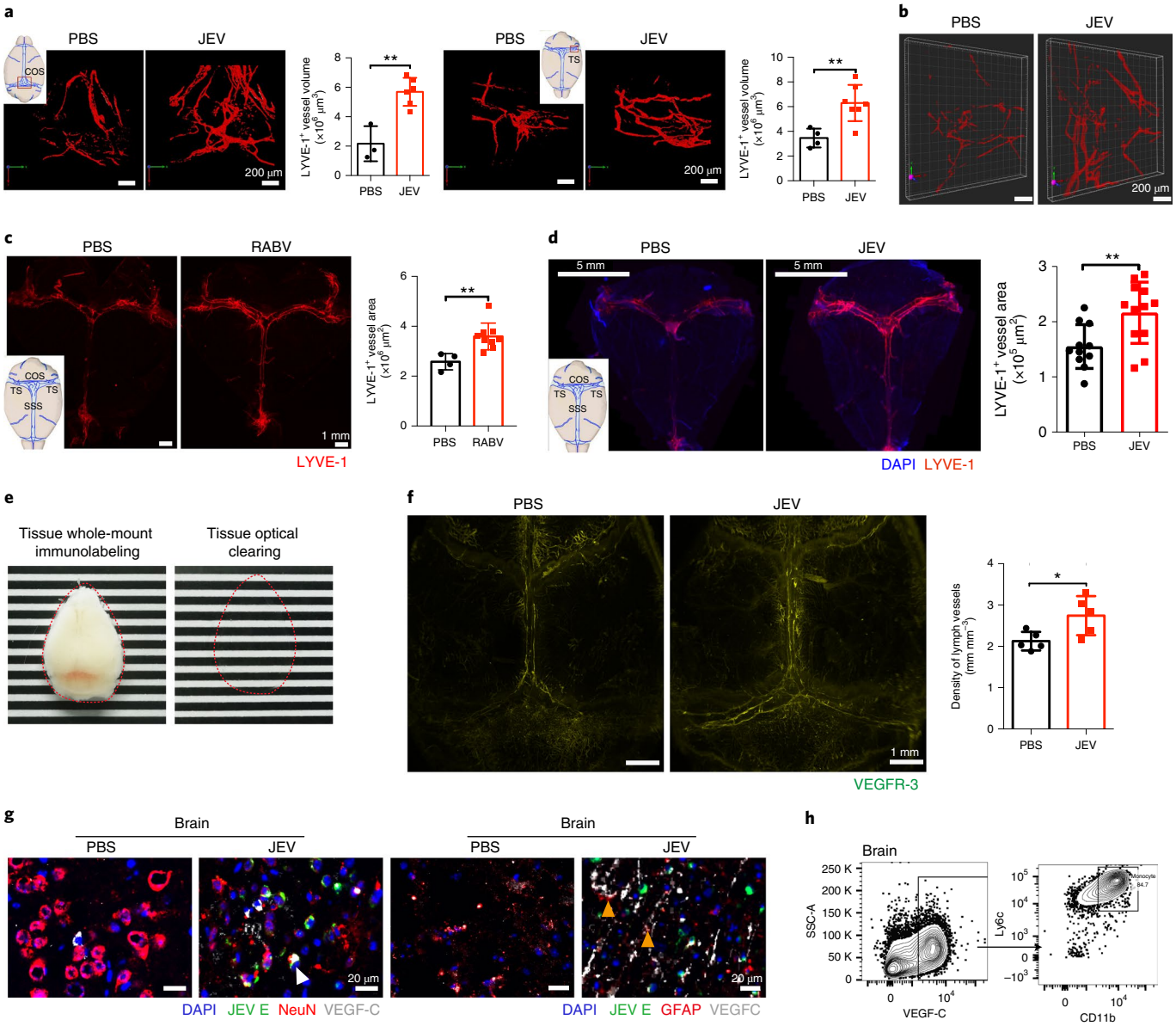

Fig. 2 | Three-dimensional imaging of meningeal lymphangiogenesis after viral infection. a,**b**, C57BL/6 mice were intravenously infected with JEV. **a**, Representative reconstruction multilayer scanning images of LYVE-1 staining and quantification of the volume of LYVE-1$^+$ MLVs around the COS and TS at 7 d.p.i. ($n=3$ or 4 PBS; $n=6$ or 7 JEV). **b**, Representative 3D image reconstruction of LYVE-1 labeling in the COS of JEV- and PBS-treated mice. See also Supplementary Video 1. **c**, Representative images of LYVE-1 staining and quantification of the area of LYVE-1$^+$ MLVs in whole-mount meninges of mice treated with RABV ($n=9$) or PBS ($n=4$). **d**, Representative images of DAPI and LYVE-1 staining and quantification of the area of LYVE-1$^+$ MLVs in whole-mount meninges of mice treated with JEV ($n=12$) or PBS ($n=11$). **e**,**f**, The MLVs of JEV- and PBS-treated mice were visualized by the volume fluorescence imaging technique. **e**, The head of a wild-type mouse before (left) and after (right) whole-mount immunolabeling and tissue optical clearing. **f**, Representative 3D projections of VEGFR-3$^+$ MLVs and quantification of the volume of VEGFR-3$^+$ MLVs in whole-mount meninges ($n=5$). See also Supplementary Video 2. **g**, Representative image of DAPI, JEV E protein, VEGF-C, NeuN and GFAP staining in the brains of PBS- or JEV-infected mice. Colocalization of JEV E protein, VEGF-C and NeuN (white arrowheads) and colocalization of JEV E protein, VEGF-C and GFAP (orange arrowheads) are shown. Data from at least three independent experiments were collected with similar results. **h**, Representative contour plots of VEGF-C$^+$Ly6c$^+$CD11b$^+$ cells in the brains of JEV-infected mice; SSC, side scatter. Data are presented as mean ± s.d.; $^*P<0.05$ and $^{**}P<0.01$ using a two-tailed, unpaired Student's *t*-test (**a**,**c**,**d** and **f**, right). Detailed statistical information is shown in Supplementary Table 2.

little was detected in JEV-infected mice. Consistently, either 60 min or 120 min after administration of OVA-647, the intensities of OVA-647 fluorescent signals in cervical regions (Fig. 3b) or around the meningeal TS region (Fig. 3c; 120 min) were still significantly weaker in JEV-infected mice than in control mice. Importantly, the fluorescent images confirmed that fluorescent signals were derived from CLNs but not other local tissues, such as superficial skin and tissue around CLNs (Fig. 3d and Extended Data Fig. 3a).

Notably, when meningeal lymphangiogenesis appeared at 3 d.p.i. with JEV (Extended Data Fig. 1f), no significant difference in OVA-647 fluorescent signal in cervical regions (Fig. 3e,f) or in the TS region of the meninges (Extended Data Fig. 3b) was

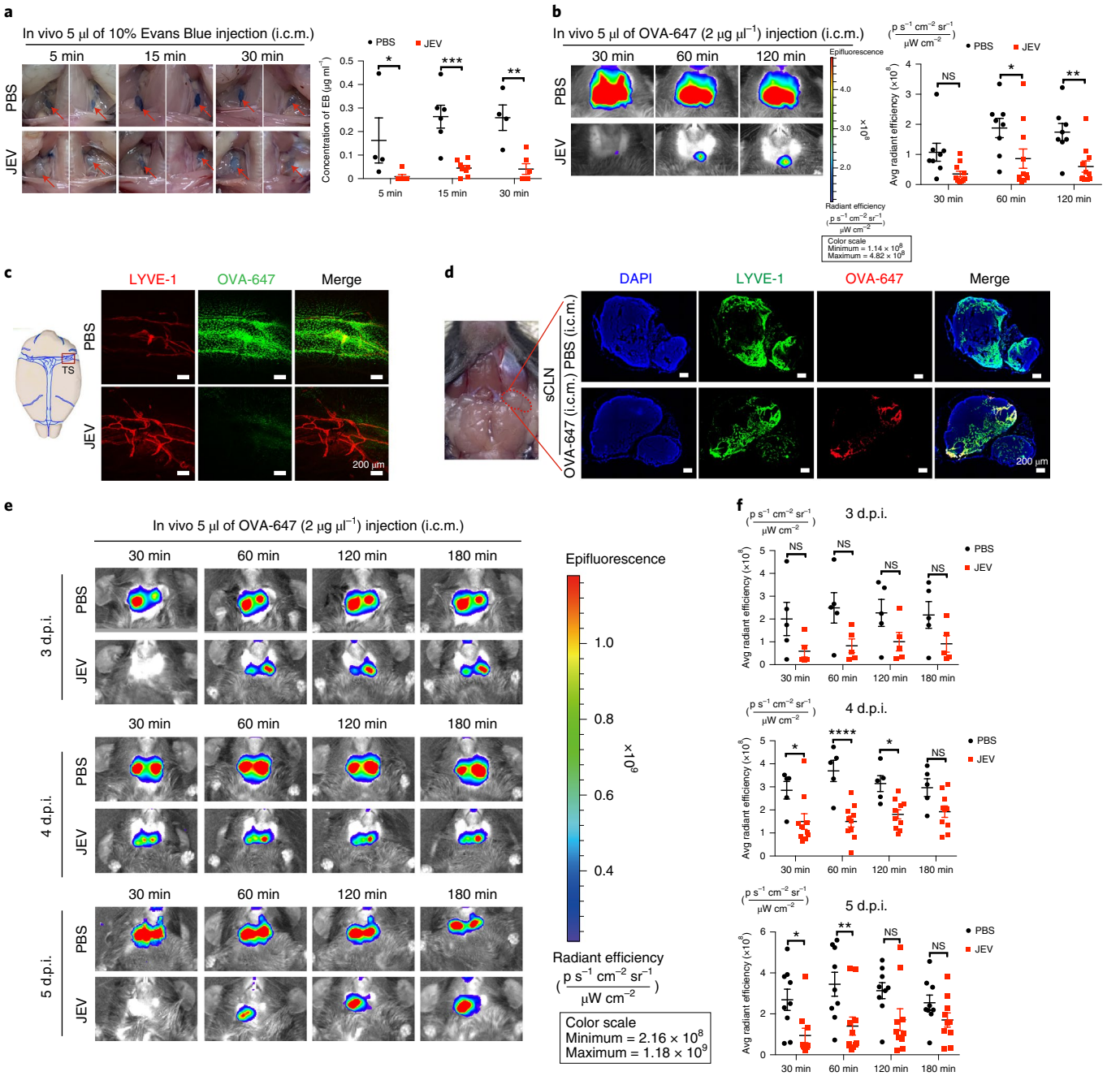

Fig. 3 | Impaired MLV ability to drain biological molecules following acute viral CNS infection. C57BL/6 mice were intravenously injected with JEV or PBS. **a**, Left, representative images of dCLNs in PBS-treated and severe JEV-treated mice at different time points after i.c.m. injection of 10% EB. Red arrows indicate the dCLNs. Right, EB concentrations in the dCLNs (5 min and 30 min: $n=4$ PBS and $n=6$ JEV; 15 min: $n=6$ PBS and $n=8$ JEV). **b**, Left, ventral images of live mice infected with PBS and JEV were captured at different time points after administration of OVA-647 using an in vivo animal imaging system. Right, fluorescence accumulation of OVA-647 in the cervical region was quantified ($n=8$ PBS; $n=11$ JEV). **c**, Representative fluorescence images of LYVE-1 staining and OVA-647 in the TS at 120 min after i.c.m. injection of OVA-647. **d**, Representative fluorescence images of DAPI and LYVE-1 staining and OVA-647 in superficial CLNs (sCLNs) at 120 min after i.c.m. injection of OVA-647 or PBS. **e**,**f**, Five microliters of OVA-647 (2 µg µl^{-1}) was injected in the i.c.m. of JEV- or PBS-treated mice at days 3, 4 or 5. Ventral images of live mice were captured at different time points (30 min, 60 min, 120 min and 180 min) after the administration of OVA-647. **e**, Ventral images show the biodistribution of OVA-647. **f**, Fluorescence accumulation of OVA-647 in the cervical region was detected in vivo on days 3, 4 and 5 after injection of JEV or PBS (day 3: $n=5$ PBS or JEV; day 4: $n=5$ PBS and $n=10$ JEV; day 5: $n=9$ PBS and $n=10$ JEV). Data are presented as mean ± s.e.m.; NS, not significant ($P>0.05$); $^{*}P<0.05$, $^{**}P<0.01$, $^{***}P<0.001$ and $^{****}P<0.0001$ using a two-way analysis of variance (ANOVA) with a Holm–Sidak multiple comparisons test (**a** (right), **b** (right) and **f**). Data are from at least two independent experiments. Detailed statistical information is shown in Supplementary Table 2.

observed between JEV-infected mice and controls. However, at days 4 and 5 after JEV infection, OVA-647 fluorescence intensities in JEV-infected mice were significantly lower than those in the control group around cervical regions (Fig. 3e,f) as well as in the TS regions (Extended Data Fig. 3b). In addition, no fluorescent signals were detected in the cervical regions at different time points after

injection of OVA-647 into the nasal mucosa of mice (Extended Data Fig. 3c), indicating that MLVs, but not nasal mucosa lymphatic vessels, represent the primary route for drainage of soluble constituents into the CLNs.

To evaluate the ability of MLVs to drain biological molecules during the recovery phase after viral infection, mice were corneally infected with HSV-1 (5,000 plaque-forming units (p.f.u.)). Some mice died about 10 d.p.i., and others suffered weight loss, edema of the head and keratitis during the acute phase (9–12 d.p.i.). Mice then gradually recovered normal weight and relief from edema and keratitis by around 28 d.p.i. (Extended Data Fig. 3d). During the acute phase of infection, OVA-647 fluorescence intensities around cervical regions were significantly lower than those in control mice (Extended Data Fig. 3e). By contrast, once HSV-1-infected mice recovered at 28 d.p.i., OVA-647 fluorescent signals in cervical regions and in the area of LYVE-1$^+$ vessels showed no significant difference compared to control mice (Extended Data Fig. 3f,g). These observations suggest that meningeal lymphangiogenesis is induced during the acute phase of viral CNS infection but returns to homeostasis during the recovery phase.

To carefully monitor MLV function, we visualized and quantitated dynamic spreading of the fluorescent nanoparticles QDot655 (QD) in MLVs in vivo through the thinned skulls of mice under two-photon fluorescence microscopy (Extended Data Fig. 3h). Lymphatic fluid flowed unimpeded in the MLVs of PBS-treated mice throughout the visualization period (Supplementary Video 3). By contrast, QD particles were congested in MLVs from JEV-infected mice and formed 'light spots' during the visualization period (Supplementary Video 3 and Extended Data Fig. 3i). Imaging of QD-congested MLVs in JEV-infected mice revealed an obvious delay of QD particle drainage (Extended Data Fig. 3i). We also observed the distribution of QD particles (i.c.m.) and blood vessels labeled with tomato lectin 488 by two-photon microscopy (Supplementary Video 4 and Extended Data Fig. 3j). These observations suggest that although MLVs are expanded in the CNS of virus-infected mice, these MLVs might lose proper function to drain soluble constituents or biological macromolecules from the CNS into CLNs.

Virus infection of the CNS causes MLV damage. Lymphatic valves and the specialized smooth muscle cells in lymphatic vessels play critical roles for lymphatic fluid transport. Muscle cells provide contractile activity to assist lymph flow[21–23], and lymphatic valves regulate the unidirectional flow of lymph to prevent backflow of fluid[24]. Transcription factors, including *Prox1*, *Gata2* and *Foxc2*, are essential to lymphatic valve development and recruitment of smooth muscle cells[1,24–29]. In addition, key regulators of cell polarity, including *Celsr1*, *Pkd1* and *Fat4*, are important for valve development[30–33]. To understand the mechanism of MLV dysfunction during viral CNS infection, we detected the expression of these genes relative to lymphatic vessel development and function. Although the gene transcripts *Celsr1*, *Pkd1*, *Sema3a*, *Egfl7*, *Fat4* and *Nrp1*, which regulate cell polarization and vascular development, were not significantly changed in MLVs following JEV infection, mRNA levels of the transcription factors *Prox1*, *Foxc2* and *Gata2* were downregulated in meninges from infected mice (Fig. 4a and Extended Data Fig. 4a). Protein expression levels of PROX1 in meninges and mRNA levels of *Prox1* and *Gata2* in CD31$^+$PDPN$^+$ LECs sorted by fluorescence-activated cell sorting (FACS) were reduced in JEV-infected mice (Fig. 4b,c). Further, fluorescence staining results showed decreased numbers of PROX1$^+$ LECs in MLVs after JEV or VSV infection (Fig. 4d,e). Consistent with our findings, previous reports have demonstrated that PROX1 was downregulated in Kaposi's sarcoma-associated herpesvirus-infected LECs in vitro[34,35]. These data suggest that viral CNS infection reduces the expression levels of *Prox1*, *Foxc2* and *Gata2* that are critical for valve function or smooth muscle cell recruitment, leading to MLV dysfunction. In addition, we found that JEV-infected hLECs upregulated the expression levels of apoptotic genes, including *BAX* and *CASP9*, although without significant changes in the expression of *BAD* and *CASP3* (Fig. 4f and Extended Data Fig. 4b). Propidium iodide (PI) staining data confirmed the increased apoptosis of hLECs following JEV infection (Fig. 4g). Taken together, these results suggest that viral CNS infection partially impairs MLV function due to a possible dysfunction of lymphatic valves and apoptosis of LECs.

MLVs drain neurotropic viral particles from the CNS to CLNs. In recent years, increasing evidence has shown the important role of MLVs in mediating CSF drainage and dissemination of intracranial cells to CLNs[4,8]. It is crucial to determine whether MLVs represent an alternative route for neurotropic viral particle spread from the CNS to CLNs. To address this, we intracerebrally injected JEV into mice and observed the accumulation of JEV virions in the dCLNs under transmission electron microscopy and by staining of the JEV E protein (Fig. 5a,b). By contrast, virions were not found in the axillary lymph nodes (AxLNs; Extended Data Fig. 5a). Suckling mice were inoculated with tissue homogenate of lymph nodes isolated from mice intracerebrally infected with JEV. The morbidity of the suckling mice that received tissue homogenate of dCLNs and sCLNs was over 40%, while mice that received tissue homogenate of mesenteric lymph nodes and AxLNs were relative healthy (Fig. 5c). These observations suggest that viruses in the CNS could be drained to CLNs and maintain infectivity.

To further assess the role of the dorsal MLVs in dissemination of virus, we surgically ligated the afferent lymphatic vessels that drain to bilateral dCLNs of mice. We then injected ZIKV or VSV–green fluorescent protein (GFP) into the cisterna magna of mice. The amount of ZIKV E protein (Fig. 5d) and VSV–GFP viral titers (Extended Data Fig. 5b) in dCLNs of the ligated mice were lower than those of the sham-treated group. To directly visualize whether MLVs were capable of carrying virus, VSV–GFP was injected into the cisterna magna of wild-type mice. At 3, 6 and 9 h after injection, colocalization of VSV–GFP and LYVE-1$^+$ MLVs was detected by confocal microscopy (Extended Data Fig. 5c), and orthogonal sectioning with *xy*, *xz* and *yz* axes was analyzed with Imaris software (Fig. 5e). To further investigate whether LECs could carry viral particles. We injected VSV–GFP into the cisterna magna of mice, and 9 h later, meninges were carefully dissected from the skull cap and stained with antibodies against PROX1 or PDPN. Colocalization of VSV–GFP and PDPN (black arrows) or PROX1 (white arrows) was also observed in meninges (Fig. 5f). These data suggest that VSV–GFP particles draining from the CNS indeed invaded MLVs. To confirm that LECs were able to carry virus, we individually infected hLECs with JEV, VSV or ZIKV for different time points. The amount of JEV, VSV or ZIKV in hLECs was increased at 24 h after infection, which further significantly enhanced at 72 h after infection (Fig. 5g). In addition, immunofluorescence analysis showed that JEV-infected hLECs could express JEV E protein (Extended Data Fig. 5d). These data demonstrate that virus can infect mLECs. Importantly, we observed LEC apoptosis following infection (Fig. 4f,g). Together, these data suggest that some virus-infected LECs are apoptotic and may enter lymphatic vessels and circulate via MLVs to CLNs. Given that MLVs are capable of carrying immune cells, it might also be possible that virus-infected immune cells carry virus and drain to the CLNs through MLVs. However, we failed to find colocalization of VSV–GFP with CD206$^+$ or with CD11b$^+$ cells in the COS of meninges 9 h after VSV–GFP was injected into the cisterna magna of mice (Extended Data Fig. 5e,f). Because VSV can infect macrophages in vitro[36,37], we suspected that some immune cells might be infected at low efficacy and could not be detected by our method in MLVs. Collectively, these findings have identified MLVs as an additional path for virus in the CNS to drain into CLNs, and virus might be transported via LECs.

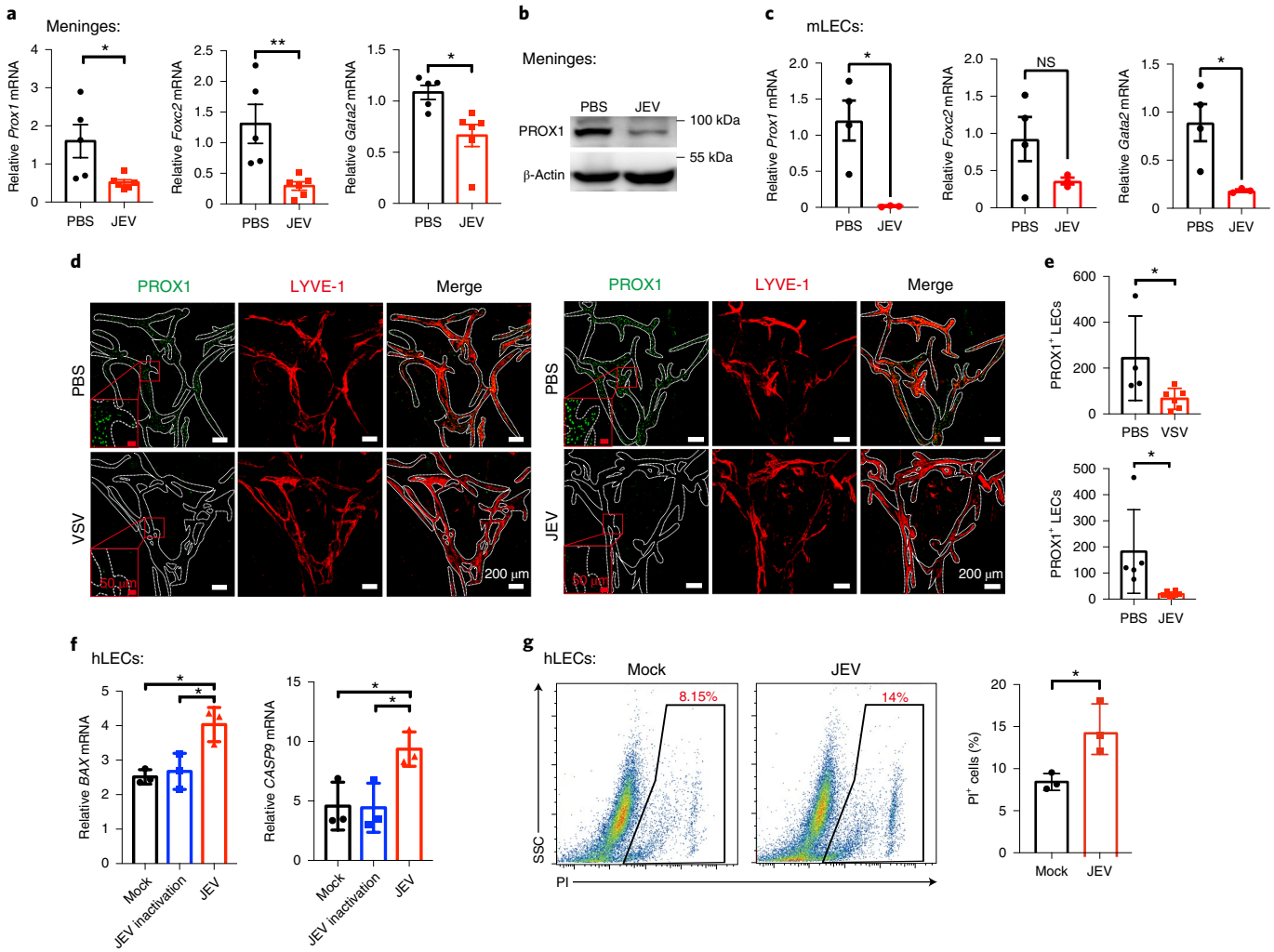

Fig. 4 | Virus infection of the CNS causes MLV damage. a, Relative mRNA levels of *Prox1*, *Foxc2* and *Gata2* in the meninges of mice treated with JEV ($n=6$) or PBS ($n=5$). **b**, Immunoblot analysis of PROX1 in the meninges of mice treated with JEV or PBS. **c**, Relative mRNA levels of *Prox1*, *Foxc2* and *Gata2* in mLECs ($CD45^-CD31^+PDPN^+$) sorted from mice treated with JEV ($n=3$) or PBS ($n=4$). **d**, Representative images of PROX1 and LYVE-1 staining in the COS of JEV-, VSV- or PBS-treated mice at 7 d.p.i. **e**, Quantification of the number of $PROX1^+$ LECs around the COS in meninges of mice treated with JEV ($n=8$), VSV ($n=6$) or PBS ($n=4$ or 5). **f**, hLECs were treated with a multiplicity of infection (MOI) of 0.1 of JEV or inactivated JEV or were untreated for 72 h. The relative mRNA levels of *BAX* and *CASP9* in hLECs are shown ($n=3$). **g**, Apoptosis of hLECs. Representative dot plots of PI^+ cells in hLECs that were treated with an MOI of 0.1 JEV for 72 h and quantification ($n=3$) are shown. Data are presented as mean ± s.e.m. (**a** and **c**) or as mean ± s.d. (**e**,**f** and **g**). NS indicates $P>0.05$; $^*P<0.05$ and $^{**}P<0.01$ as assessed by two-tailed, unpaired Student's *t*-test (**a**,**c**,**e** and **g** (right)) and one-way ANOVA with Holm–Sidak multiple comparisons test (**f**). Detailed statistical information is shown in Supplementary Table 2.

To investigate whether viral antigen from the CNS-infected brain was presented by antigen-presenting cells (APCs) in the draining lymph nodes, mice were intracerebrally injected with JEV or PBS. dCLN sections were immunostained with anti-JEV E protein, anti-major histocompatibility complex class II (MHC class II), anti-CD86 and DAPI. JEV E protein colocalized with MHC class II^+ cells (Fig. 5h), and we confirmed that B cells and monocytes in dCLNs and sCLNs significantly upregulated the expression of CD86 and CD80, but this did not occur in AxLNs (Fig. 5i and Extended Data Fig. 5g–i). These data suggest that after viral invasion of the brain, viral antigen could be presented by MHC class II^+ cells in the draining lymph nodes, and professional APCs, including B cells and monocytes, are activated with enhanced CD80/CD86 expression for T cell activation.

MLV ablation or VEGF-C treatment affects mouse mortality. Next, we asked whether meningeal lymphatic drainage affected viral clearance and the survival of infected hosts because the function of MLVs was partially destroyed after viral infection of the CNS. Surgical ligation of afferent lymphatic vessels reaching the dCLNs was performed followed by JEV infection, which significantly aggravated mortality of JEV-infected mice (Fig. 6a,b). Additionally, MLVs were subjected to ablation using a Visudyne-based approach[4], and the efficient elimination of MLVs around the COS and TS was confirmed (Fig. 6c). Ablation of MLVs also significantly enhanced the mortality of JEV-infected mice (Fig. 6d) and increased viral burden in the cerebellum and brainstem (Fig. 6e). Flow cytometry showed that in MLV-ablated mice, numbers of immune cells, including $CD45^+$ cells, neutrophils, macrophages, monocytes, $CD8^+$ T cells and natural killer (NK) cells, were all significantly increased in the brain following JEV infection (Fig. 6f and Extended Data Fig. 6). In agreement, expression levels of inflammatory cytokines, such as *Il6*, *Tnfa*, *Il1b* and *Ccl5*, were enhanced in the brain after ablation of lymphatic vessels (Fig. 6g,h). These results suggest that excessive inflammatory damage in the CNS might account for increased mortality when MLVs are ablated.

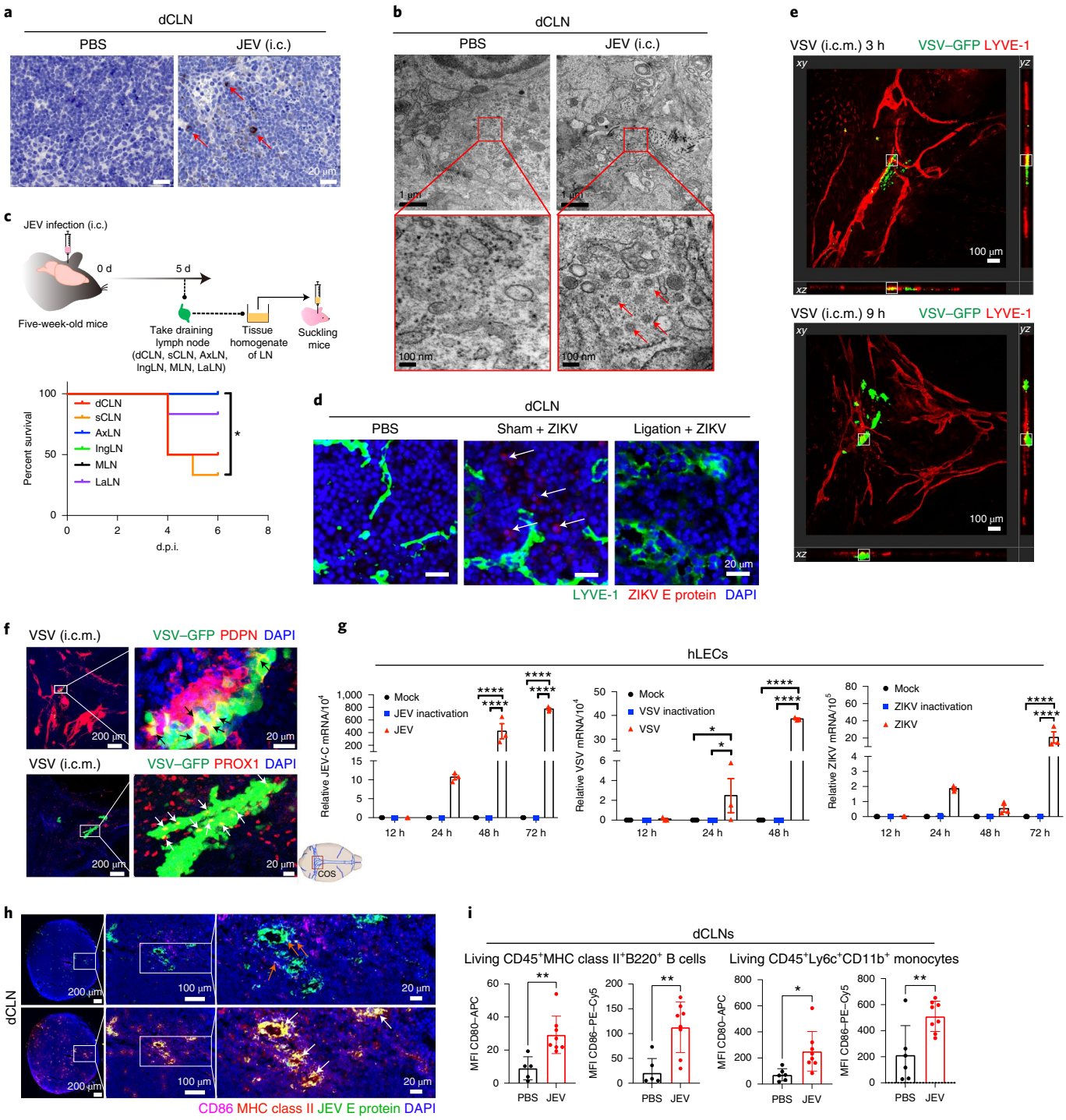

Fig. 5 | MLVs drain neurotropic viral particles from the CNS to CLNs. a–**c**, Mice were intracerebrally (i.c.) injected with JEV or PBS. **a**, Representative images of JEV E protein immunohistochemical staining (red arrows) in the dCLN. **b**, A JEV virion (red arrows) in the dCLN in a mouse with severe JEV infection was imaged by transmission electron microscopy. **c**, The dCLN, sCLN, AxLN, inguinal lymph node (IngLN), mesenteric lymph node (MLN) and lumbar artery lymph node (LaLN) were collected, and suckling mice were intracerebrally challenged with the tissue homogenate from above-mentioned lymph nodes and monitored for survival. **d**, Representative images of DAPI, LYVE-1 and ZIKV E protein (white arrows) staining in the dCLN from mice treated with PBS or ZIKV via intracerebral injection with ligation or non-ligation of deep cervical lymphatic vessels. **e**,**f**, VSV-GFP was i.c.m. injected. **e**, Orthogonal sections showing VSV-GFP overlapping with LYVE-1 signals on the COS and TS from the *xy*, *yz* and *xz* axes. **f**, Representative images of DAPI, VSV-GFP, PDPN and PROX1 staining in the COS of meninges at 9 h after VSV-GFP injection. Colocalization of VSV-GFP with PDPN (black arrows) or with PROX1 (white arrows) is shown in the magnified images. **g**, hLECs were treated with an MOI of 0.1 JEV or inactivated JEV, an MOI of 0.01 VSV or inactivated VSV or an MOI of 0.1 ZIKV or inactivated ZIKV or were untreated for different amounts of time. Viral mRNA from JEV-C, VSV or ZIKV was detected ($n=3$). **h**,**i**, Mice were intracerebrally injected with JEV. **h**, Representative images of DAPI, JEV E protein, MHC class II and CD86 staining in the dCLN. Colocalization of JEV E protein and MHC class II (white arrows) or CD86 (orange arrows) is shown in the magnified images. **i**, The mean fluorescence intensity (MFI) of CD86 and CD80 on B cells or monocytes was quantified in dCLNs ($n=5$ or 6 PBS; $n=8$ JEV). Data are presented as mean ± s.d.; $^{*}P<0.05$, $^{**}P<0.01$ and $^{****}P<0.0001$ as determined by log rank (Mantel–Cox) test (**c**), two-way ANOVA with Holm–Sidak multiple comparisons test (**g**) or two-tailed unpaired Student's *t*-test (**i**). Data are from at least two independent experiments. Detailed statistical information is shown in Supplementary Table 2.

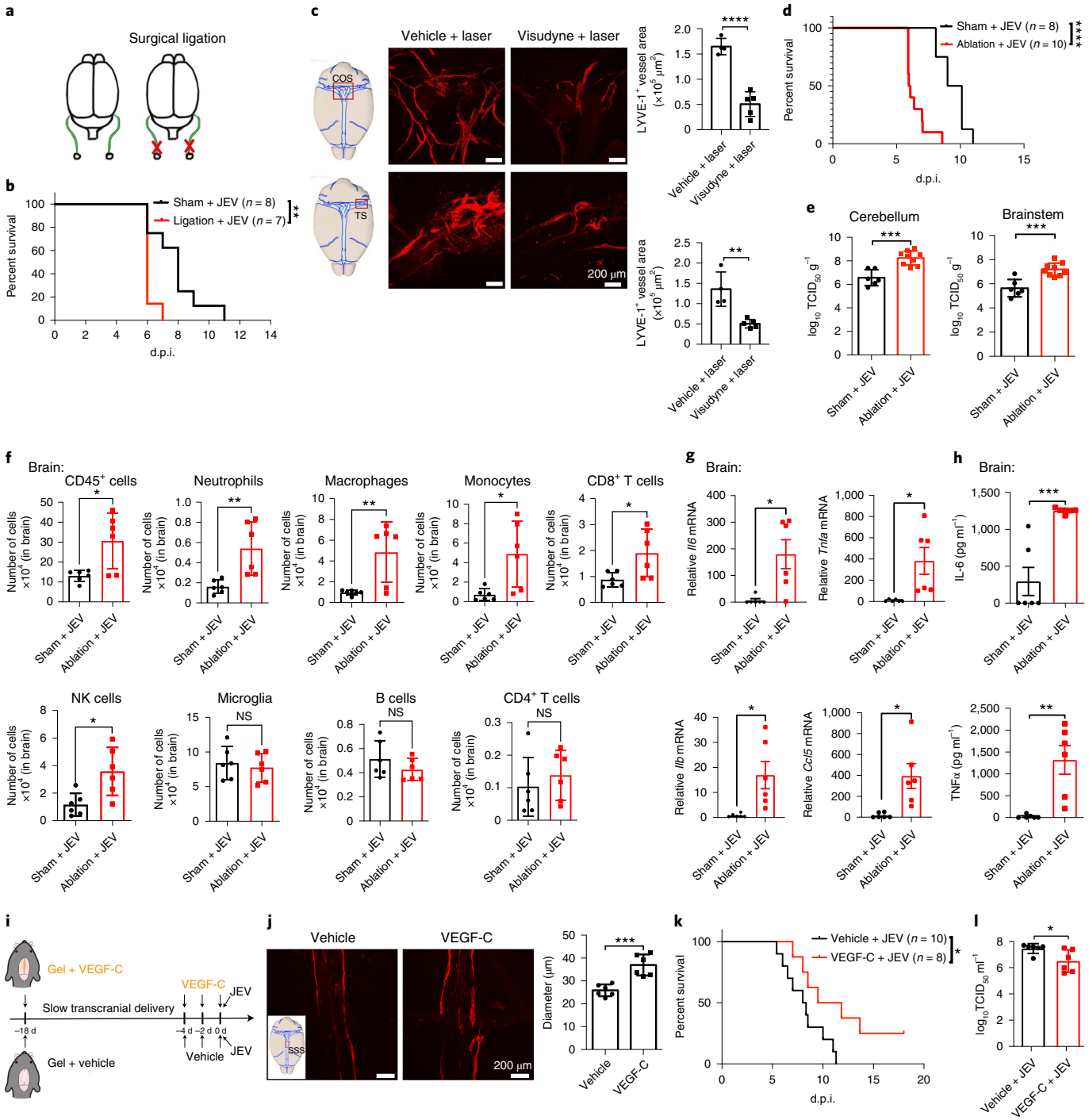

Fig. 6 | Ablation of lymphatic drainage enhances, but VEGF-C pretreatment reduces, mortality of JEV-infected mice. a,**b**, Lymphatic vessels of the dCLN were ligated (**a**), and 7 d later, mice were intravenously challenged with JEV. Survival curves of JEV-infected mice ($n = 8$ sham; $n = 7$ ligation) are shown (**b**). **c**–**h**, Mice were treated with vehicle and laser or Visudyne and laser (to ablate dorsal MLVs). Seven days later, mice were intravenously infected with JEV. **c**, Representative image of meningeal LYVE-1 staining and quantification of the area of LYVE-1$^+$ MLVs in the COS and TS 1 week after mice were treated ($n = 4$ vehicle and laser; $n = 5$ Visudyne and laser). **d**, Survival curves of JEV-infected mice ($n = 8$ sham; $n = 10$ ablation). **e**, Viral titer was measured by 50% tissue culture infective dose ($TCID_{50}$) assay ($n = 6$ sham; $n = 9$ ablation). **f**, Absolute numbers of CD45$^+$ cells, neutrophils, macrophages, monocytes, CD8$^+$ T cells, CD4$^+$ T cells, NK cells, microglia and B cells in the brain ($n = 6$). **g**, mRNA levels of inflammatory factors in the brain at 4 d.p.i. ($n = 6$). **h**, IL-6 and TNFα concentration in the brain at 4 d.p.i. ($n = 6$). **i**–**l**, Hydrogel alone (vehicle) or containing recombinant human VEGF-C (200 ng ml^{-1}) was applied on top of a thinned skull surface on mice. VEGF-C was injected subcutaneously into the head three times 2 weeks later. Seven days later, mice were intravenously challenged with JEV (**i**). Representative images of LYVE-1 staining and quantification of the diameter of LYVE-1$^+$ MLVs in the SSS ($n = 6$) are shown (**j**). Survival curves of JEV-infected mice ($n = 10$ PBS; $n = 8$ VEGF-C) are also displayed. Viral burden was measured by $TCID_{50}$ assay from the brain (**l**; $n = 6$). Data are presented as mean ± s.d. (**c**,**e**,**f**, **j** and **l**) or as mean ± s.e.m. (**g** and **h**). NS indicates $P > 0.05$; $^*P < 0.05$, $^{**}P < 0.01$, $^{***}P < 0.001$ and $^{****}P < 0.0001$. P values were determined by two-tailed unpaired Student's t-test (**c** (right), **e**,**f**,**g**,**h**,**j** (right) and **l**) or by log rank (Mantel–Cox) test (**b**,**d** and **k**). Detailed statistical information is shown in Supplementary Table 2.

Previous reports have shown that treatment with recombinant VEGF-C increased the diameter of MLVs and that VEGF-C can synergize with immune checkpoint blockade in the treatment of brain tumors[6–8]. To evaluate the effect of VEGF-C treatment against viral CNS infection, we applied hydrogel-encapsulated recombinant VEGF-C peptide and pretreated mice four times, as indicated in Fig. 6i, followed by JEV infection. We confirmed that VEGF-C pretreatment increased the diameter of meningeal lymphatics in mice (Fig. 6j), consistent with a previous finding showing that VEGF-C administration could expand meningeal lymphatics with normal function[6]. Indeed, VEGF-C pretreatment significantly improved the survival of JEV-infected mice, with reduced viral loads observed in the brain (Fig. 6k,l). These results suggest that VEGF-C pretreatment might promote the formation of functional MLVs to protect the host against neurotropic viral infection. In addition to regulating lymphatic function, our previous work has demonstrated that VEGF-C can regulate macrophage-induced responses to infection. We reported that VEGF-C inhibits TLR4-induced excessive inflammation and septic shock during bacterial infection[38]. We also demonstrated that macrophages use the VEGFR-3/VEGF-C module to enhance phagocytosis and bacterial clearance while inhibiting inflammasome activation and macrophage pyroptosis[39]. Together with our observation that MLV-ablated mice show significantly enhanced numbers of macrophages, monocytes, NK cells, $CD4^+$ T cells and $CD8^+$ T cells in the brain (Fig. 6f), these findings suggest that VEGF-C pretreatment might ameliorate the severity of viral CNS infection by affecting lymphangiogenesis as well as immune responses.

Discussion

Infection can be controlled locally or can spread systemically. Previous studies have shown that serious infection can increase the permeability of the BBB, allowing virus to enter into the brain via the BBB and leading to the release of inflammatory mediators[14,15,40,41]. Here, we have provided evidence that CNS-invading neurotropic viruses use MLVs as an additional path to spread toward the CLNs. We found that viral infection in the CNS promotes meningeal lymphangiogenesis, with partially impaired MLVs functioning to drain virus or macromolecules. Viruses can infect hLECs in vitro, and virus-invaded LECs facilitate virus transfer from the CNS to MLVs in vivo. Additionally, the specific photodynamic ablation of dorsal MLVs or ligation of dCLNs significantly exacerbated neurological damage and mortality during viral infection in mice. VEGF-C pretreatment caused expansion of functional MLVs and alleviated CNS damage of virus-infected mice. Taken together, our study has revealed that MLVs support the spread of viruses from the CNS to the periphery, and VEGF-C-induced expansion of functional MLVs could protect against neurological damage during viral CNS infection.

Recently, the existence and function of the meningeal lymphatic network in the brain has been suggested to carry CSF components along with immune cells from the CNS to CLNs under various pathological conditions, including Alzheimer's disease, multiple sclerosis, stroke and brain tumors[4–9,42–44]. In this study, we speculate that once virus spreads from the CNS to the periphery via MLVs, viruses might then be detected and cleared by immune cells in the CLNs based on the following observation. After viral CNS infection, some macrophages and B cells in CLNs are colocalized together with virus and upregulate the expression of costimulatory molecules CD80/CD86 (Fig. 5h,i). It is possible that at the initial infection stage when the BBB is intact, virus might spread in low amounts and reach the CLNs, where APCs would present viral antigens to activate T cells. These activated immune cells may not only clear viruses in the CLNs but also migrate through the MLVs into the CNS to eliminate more viruses and terminate infection. Future investigation might address whether functional MLVs are one of the critical tunnels promoting immune elimination of viral infections. Because virus could be transported from the CNS to CLNs through MLVs, another key question was raised about how the CNS drains virus through MLVs. In this study, we have provided evidence showing that neurotropic viruses could efficiently infect LECs in the meninges of the mouse brain in vivo and in hLECs in vitro (Fig. 5e–g), and virus-infected LECs undergo apoptosis. It is therefore possible that viruses invading the brain might infect adjacent mLECs and become transported together with apoptotic LECs via MLVs and drained into CLNs. In addition, previous reports suggest that immune cells could be drained in MLVs from the brain[4,45]. It is reasonable to speculate that if viruses infect immune cells in the brain, viruses might be transported together with immune cells to the CLNs. Although our results did not identify viral infection of $CD11b^+$ and $CD206^+$ cells in meninges under these experimental conditions (Extended Data Fig. 5e,f), we cannot rule out that some viruses might infect other immune cells besides $CD206^+$ or $CD11b^+$ cells or might infect these immune cells with low efficacy that could not be detected by our method. Further investigation as to whether infiltrating immune cells act as carriers to transport viruses via MLVs should be explored using additional methods, such as spatial transcriptomics.

Our study also observed that, although viral infection could promote the formation of MLVs, the ability to transport components from the CNS to CLNs is impaired. Notably, it was reported that neuroinflammation could induce lymphangiogenesis near the cribriform plate, which contributes to drainage of fluid, cells and antigen[9]. In contrast to the newly formed functional dorsal lymphatic vessels, basal MLVs in aged mice increase in size along with highly branched and hyperplastic phenotypes and reduced capability of transporting QD705 tracers injected into the cisterna magna[1]. These reports show that different function of the newly formed lymphatic vessels might be due to different disease conditions or distinct sublocations of MLVs in the brain. *Prox1*, *Foxc2* and *Gata2* are essential for the formation of lymphatic valves and the recruitment of smooth muscle cells attached to lymphatic vessels, which are needed for lymphatic transport[23–29]. Previous studies demonstrated that downregulation of PROX1 and FOXC2 expression in meningeal lymphatic valves in aging mice could lead to reduced lymphatic valves and reduced QD705 tracer transport[1]. In agreement with these findings, we found that expression of PROX1 in MLVs and transcription of *Foxc2* and *Gata2* in viral-infected mLECs were significantly downregulated. In addition, we observed enhanced apoptosis of hLECs following viral infection (Fig. 4f,g). Therefore, dysfunction of MLVs in viral infection could be due to LEC apoptosis and destroyed integrity as well as the impaired formation of lymphatic valves by viral infection. Except for the reasons explained above, viral CNS infection could release multiple stress signals and cause diverse changes, such as neurotransmitters in the CNS microenvironment. Further investigations are needed to identify key effectors and the underlying mechanisms that could explain MLV dysfunction and CNS damage. Accordingly, what other components could be cleared from the CNS to protect the host during viral infection or in the development of neurological diseases? To maintain brain homeostasis, could MLVs take up and transport metabolic waste, misfolded proteins, apoptotic cells and cytokines that are produced at excessive levels out of the CNS? With this new understanding, the MLV network might be a targeted route in the resolution of neurological disease.

In summary, our study proposes the following features of MLVs following acute viral infection: (1) MLVs can transport virus from the CNS to draining CLNs, (2) VEGF-C pretreatment promotes functional MLV formation in the CNS against viral infection, suggesting a promising therapeutic approach against neurotropic viral infection, and (3) although neurotropic virus infection promotes MLV formation in the CNS, MLV function is impaired.

Online content

Any methods, additional references, Nature Research reporting summaries, source data, extended data, supplementary information, acknowledgements, peer review information; details of author contributions and competing interests; and statements of data and code availability are available at https://doi.org/10.1038/s41593-022-01063-z.

Received: 8 May 2021; Accepted: 24 March 2022;
Published online: 6 May 2022

References

1. Ahn, J. H. et al. Meningeal lymphatic vessels at the skull base drain cerebrospinal fluid. *Nature* **572**, 62–66 (2019).
2. Louveau, A. et al. Structural and functional features of central nervous system lymphatic vessels. *Nature* **523**, 337–341 (2015).
3. Aspelund, A. et al. A dural lymphatic vascular system that drains brain interstitial fluid and macromolecules. *J. Exp. Med.* **212**, 991–999 (2015).
4. Louveau, A. et al. CNS lymphatic drainage and neuroinflammation are regulated by meningeal lymphatic vasculature. *Nat. Neurosci.* **21**, 1380–1391 (2018).
5. Louveau, A., Da Mesquita, S. & Kipnis, J. Lymphatics in neurological disorders: a neuro–lympho–vascular component of multiple sclerosis and Alzheimer's disease? *Neuron* **91**, 957–973 (2016).
6. Da Mesquita, S. et al. Functional aspects of meningeal lymphatics in ageing and Alzheimer's disease. *Nature* **560**, 185–191 (2018).
7. Song, E. et al. VEGF-C-driven lymphatic drainage enables immunosurveillance of brain tumours. *Nature* **577**, 689–694 (2020).
8. Hu, X. T. et al. Meningeal lymphatic vessels regulate brain tumor drainage and immunity. *Cell Res.* **30**, 229–243 (2020).
9. Hsu, M. et al. Neuroinflammation-induced lymphangiogenesis near the cribriform plate contributes to drainage of CNS-derived antigens and immune cells. *Nat. Commun.* **10**, 229 (2019).
10. Silva, M. T. T. Viral encephalitis. *Arq. Neuropsiquiatr.* **71**, 703–709 (2013).
11. Solomon, T. Flavivirus encephalitis—reply. *N. Engl. J. Med.* **351**, 1804–1804 (2004).
12. Tyler, K. L. Herpes simplex virus infections of the central nervous system: encephalitis and meningitis, including Mollaret's. *Herpes* **11**, 57A-64A (2004).
13. Moseman, E. A., Blanchard, A. C., Nayak, D. & McGavern, D. B. T cell engagement of cross-presenting microglia protects the brain from a nasal virus infection. *Sci Immunol.* **5**, eabb1817 (2020).
14. Patabendige, A., Michael, B. D., Craig, A. G. & Solomon, T. Brain microvascular endothelial–astrocyte cell responses following Japanese encephalitis virus infection in an in vitro human blood–brain barrier model. *Mol. Cell Neurosci.* **89**, 60–70 (2018).
15. Mustafa, Y. M., Meuren, L. M., Coelho, S. V. A. & de Arruda, L. B. Pathways exploited by flaviviruses to counteract the blood–brain barrier and invade the central nervous system. *Front. Microbiol.* **10**, 525 (2019).
16. Luo, Z. C. et al. Dual role of Toll-like receptor 7 in the pathogenesis of rabies virus in a mouse model. *J. Virol.* **94**, e00111-20 (2020).
17. Wang, W. et al. Zika virus infection induces host inflammatory responses by facilitating NLRP3 inflammasome assembly and interleukin-1β secretion. *Nat. Commun.* **9**, 106 (2018).
18. Renier, N. et al. Mapping of brain activity by automated volume analysis of immediate early genes. *Cell* **165**, 1789–1802 (2016).
19. Liu, T. et al. Local sympathetic innervations modulate the lung innate immune responses. *Sci. Adv.* **6**, eaay1497 (2020).
20. Cao, Y., Wang, H. & Zeng, W. Whole-tissue 3D imaging reveals intra-adipose sympathetic plasticity regulated by NGF–TrkA signal in cold-induced beiging. *Protein Cell* **9**, 527–539 (2018).
21. Lutter, S., Xie, S., Tatin, F. & Makinen, T. Smooth muscle-endothelial cell communication activates Reelin signaling and regulates lymphatic vessel formation. *J. Cell Biol.* **197**, 837–849 (2012).
22. Wang, Y. et al. Molecular and cellular basis of the regulation of lymphatic contractility and lymphatic absorption. *Int. J. Biochem. Cell Biol.* **53**, 134–140 (2014).
23. Muthuchamy, M. & Zawieja, D. Molecular regulation of lymphatic contractility. *Ann. N. Y. Acad. Sci.* **1131**, 89–99 (2008).
24. Petrova, T. V. et al. Defective valves and abnormal mural cell recruitment underlie lymphatic vascular failure in lymphedema distichiasis. *Nat. Med.* **10**, 974–981 (2004).
25. Sabine, A. et al. Mechanotransduction, PROX1, and FOXC2 cooperate to control connexin37 and calcineurin during lymphatic-valve formation. *Dev. Cell* **22**, 430–445 (2012).
26. Norrmen, C. et al. FOXC2 controls formation and maturation of lymphatic collecting vessels through cooperation with NFATc1. *J. Cell Biol.* **185**, 439–457 (2009).
27. Srinivasan, R. S. & Oliver, G. *Prox1* dosage controls the number of lymphatic endothelial cell progenitors and the formation of the lymphovenous valves. *Gene Dev.* **25**, 2187–2197 (2011).
28. Kazenwadel, J. et al. GATA2 is required for lymphatic vessel valve development and maintenance. *J. Clin. Invest.* **125**, 2979–2994 (2015).
29. Kazenwadel, J. et al. Loss-of-function germline *GATA2* mutations in patients with MDS/AML or MonoMAC syndrome and primary lymphedema reveal a key role for GATA2 in the lymphatic vasculature. *Blood* **119**, 1283–1291 (2012).
30. Tatin, F. et al. Planar cell polarity protein Celsr1 regulates endothelial adherens junctions and directed cell rearrangements during valve morphogenesis. *Dev. Cell* **26**, 31–44 (2013).
31. Alders, M. et al. Hennekam syndrome can be caused by *FAT4* mutations and be allelic to Van Maldergem syndrome. *Hum. Genet.* **133**, 1161–1167 (2014).
32. Betterman, K. L. et al. Atypical cadherin FAT4 orchestrates lymphatic endothelial cell polarity in response to flow. *J. Clin. Invest.* **130**, 3315–3328 (2020).
33. Coxam, B. et al. Pkd1 regulates lymphatic vascular morphogenesis during development. *Cell Rep.* **7**, 623–633 (2014).
34. Yoo, J. et al. Opposing regulation of PROX1 by interleukin-3 receptor and NOTCH directs differential host cell fate reprogramming by Kaposi sarcoma herpes virus. *PLoS Pathog.* **8**, e1002770 (2012).
35. Gramolelli, S. et al. Oncogenic herpesvirus engages endothelial transcription factors SOX18 and PROX1 to increase viral genome copies and virus production. *Cancer Res.* **80**, 3116–3129 (2020).
36. Xiao, J. et al. Targeting 7-dehydrocholesterol reductase integrates cholesterol metabolism and IRF3 activation to eliminate infection. *Immunity* **52**, 109–122 (2020).
37. Zhang, C. et al. Targeting lysophospholipid acid receptor 1 and ROCK kinases promotes antiviral innate immunity. *Sci. Adv.* **7**, eabb5933 (2021).
38. YanboZhang et al. Activation of vascular endothelial growth factor receptor-3 in macrophages restrains TLR4–NF-κB signaling and protects against endotoxin shock. *Immunity* **40**, 501–514 (2014).
39. Ma, L. et al. FLT4/VEGFR3 activates AMPK to coordinate glycometabolic reprogramming with autophagy and inflammasome activation for bacterial elimination. *Autophagy* **2021**, 1–16, (2021).
40. Cle, M. et al. Zika virus infection promotes local inflammation, cell adhesion molecule upregulation, and leukocyte recruitment at the blood–brain barrier. *mBio* **11**, e01183-20 (2020).
41. Carvalho, G. C. D. et al. RAGE and CCR7 mediate the transmigration of Zika-infected monocytes through the blood–brain barrier. *Immunobiology* **224**, 792–803 (2019).
42. Weller, R. O., Galea, I., Carare, R. O. & Minagar, A. Pathophysiology of the lymphatic drainage of the central nervous system: implications for pathogenesis and therapy of multiple sclerosis. *Pathophysiology* **17**, 295–306 (2010).
43. Raper, D., Louveau, A. & Kipnis, J. How do meningeal lymphatic vessels drain the CNS? *Trends Neurosci.* **39**, 581–586 (2016).
44. Noé, F. M. & Marchi, N. Central nervous system lymphatic unit, immunity, and epilepsy: is there a link? *Epilepsia Open* **4**, 30–39 (2019).
45. Brioschi, S. et al. Heterogeneity of meningeal B cells reveals a lymphopoietic niche at the CNS borders. *Science* **373**, eabf9277 (2021).

Publisher's note Springer Nature remains neutral with regard to jurisdictional claims in published maps and institutional affiliations.

© The Author(s), under exclusive licence to Springer Nature America, Inc. 2022

Methods

Ethics approval. The animal experiments (JEV, ZIKV, VSV and HSV-1 infection) described in the study were preapproved by the Ethical Committee for Animal Experiments of Wuhan Institute of Virology (protocol numbers WIVA39201602, WIVA39201603, WIVA39201803 and WIVA39201804). Animal experiments involving RABV infection described in the study were preapproved by the Scientific Ethics Committee of Huazhong Agricultural University (permit number HZAUMO-2016-052).

Animals. The studies described here used 5- to 8-week-old male and female C57BL/6J mice. Experiments involving ZIKV infection used 5-week-old AG6 mice of both sexes. Specific pathogen-free C57BL/6J adult mice of both sexes were purchased from Beijing Vital River Laboratory Animal Technology. AG6 mice with the strain 129 background have been backcrossed onto the C57BL/6 background for more than six generations and were a kind gift from Q. Leng of the Institute Pasteur of Shanghai, Chinese Academy of sciences (CAS). Animal care and experimental procedures were performed in an Animal Biological Safety Level 2 laboratory at the Wuhan Institute of Virology, CAS. All mice had free access to a standard diet and water and were housed on a 12-h light/12-h dark cycle in rooms maintained at 20 °C and 55% humidity. Mice were anesthetized with intraperitoneal injection of a combination of anesthetics before all experiments.

Cells and viruses. BHK-21 cells were provided by S. Cao of Huazhong Agricultural University, and 293T cells were provided by H. Wang of Shanghai Institute of Biochemistry and Cell Biology. C6/36 cells were provided by H. Yan of Wuhan Institute of Virology. Vero-E6 cells were obtained from the National Collection of Authenticated Cell Cultures (GNO17). BHK-21, Vero-E6 and 293T cells were cultured in Dulbecco's modified Eagle's medium (DMEM; Sigma) containing 10% fetal bovine serum (FBS; Gibco) and 100 U ml^{-1} of penicillin/streptomycin at 37 °C with 5% CO_2. C6/36 cells were cultured in 1640 medium (Gibco) containing 10% FBS at 28 °C. hLECs were obtained from ScienCell (2500). Cells were seeded in 24-well Nunc plates and coated with 0.1% gelatin (Difco, 214340). Culture medium was complete endothelial cell medium (ScienCell, 1001) containing 5% FBS, 1% endothelial cell growth supplement and 1% penicillin/streptomycin at 37 °C under 5% CO_2 conditions. Subculturing was performed when cultures reached 90% confluency.

The RABV CVS-B2C strain was provided by the laboratory of L. Zhao of Huazhong Agricultural University. ZIKV was provided by the laboratory of H. Wang of the Wuhan Institute of Virology, CAS, and propagated in C6/36 cells. HSV-1 was provided by the laboratory of Z. Qian of Institute Pasteur of Shanghai, CAS, and propagated in Vero-E6 cells. VSV–GFP was supplied by the laboratory of M. Jin of Huazhong Agricultural University and propagated in the 293T cells. The JEV P3 strain was provided by S. Cao of Huazhong Agricultural University and propagated in the brains of suckling mice. Virus stocks were titrated by conventional plaque assay or $TCID_{50}$ assay and were stored in aliquots at −80 °C until use.

Quantitative real-time PCR (qRT–PCR). Relative mRNA expression levels of target genes were measured by qRT–PCR. Total RNA was extracted from cells or tissues with Trizol reagent (Vazyme), and cDNA was generated using a reverse transcriptase M-MLV kit (Takara). Relative qRT–PCR was performed on a Stratagene MX3000P real-time PCR system (Agilent Technologies) with Cham QTM qRT–PCR SYBR Green master mix (Vazyme). The $2^{-\Delta\Delta C_t}$ method was used to calculate relative gene expression levels. *Gapdh* was amplified as an internal control. Sequences of all primers are listed in Supplementary Table 1.

Enzyme-linked immunosorbent assay (ELISA). Concentrations of VEGF-C, TNFα and IL-6 were measured by ELISA commercial kits according to the manufacturer's instructions.

$TCID_{50}$ assay. JEV titer was measured by $TCID_{50}$ as previously described[46]. Supernatant fluids of brain homogenate in PBS from JEV-infected mice were collected and serially diluted tenfold. Samples (100 µl) of each dilution were added to duplicate wells of a 96-well plate containing 70% confluent BHK-21 cells. Five days were allowed for the appearance of cytopathology. The dilution causing cytopathology in half of the cultures (the median $TCID_{50}$) was calculated by the Reed–Muench method.

Plaque assay. For VSV plaque assays, the supernatant of lymph node homogenates from mice infected with VSV were collected and diluted 1:10 to $1:10^4$ in DMEM and were used for infection of Vero-E6 cells plated on 12-well plates. At 3 h after infection, the supernatants were removed, and cells were washed with PBS twice. DMEM containing 1% low melting agar and 2% FBS was overlaid onto the cells. At 3 d.p.i., cells were fixed for 20 min with 4% formaldehyde and stained with 0.2% crystal violet. Plaques were counted and averaged, and results were multiplied by the dilution factor to calculate viral titers as p.f.u. per ml.

Immunohistochemistry. Lymph nodes were embedded in paraffin after fixation in 4% paraformaldehyde (PFA). Tissue sections were stained with anti-JEV E (from C. Gu of Huazhong Agricultural University). Stained sections were scanned and analyzed using a Zeiss Axio Scan.Z1.

Transmission electron microscopy. For transmission electron microscopy, dCLNs were collected and fixed with 2.5% glutaraldehyde. After rinsing in buffer, the tissue was dehydrated through a series of graded ethanol, infiltrated and embedded in Epon 812 and polymerized at 60 °C for 48 h. Sections (0.3 mm) were stained with toluidine blue for light microscopy examination. Ultrathin sections (70 nm) were cut with a Diatome diamond knife on a Reichert-Jung Ultracut ultramicrotome (Leica EM UC7). Ultrathin sections were mounted on 200-mesh copper grids and stained with Reynold's lead citrate stain. Images were captured using an FEI Tecnai G2 Spirit Twin transmission electron microscope at 80 kV.

Volume fluorescence imaging. Volume fluorescence imaging of MLVs was performed as recently reported[20]. Mice of the indicated conditions were anesthetized and perfused with 25 ml of PBS, followed by 25 ml of PBS/1% PFA. Brains without skin were removed and fixed in PBS/1% PFA at 4 °C for 6 h. Tissues were washed with PBS for 30 min three times. Tissues were decalcified in 350 mM EDTA-Na (pH 6.5) at 37 °C for 72 h, with fresh buffer changed every 24 h.

The decalcified tissues were dehydrated at room temperature in 20% methanol for 2 h, 40% methanol for 2 h, 60% methanol for 2 h, 80% methanol for 2 h and 100% methanol for 2 h twice. Tissues were then bleached at 4 °C overnight with a mixture of 30% hydrogen peroxide and 100% methanol (1 vol of 30% hydrogen peroxide diluted in 10 vol of 100% methanol) and rehydrated at room temperature in 100% methanol for 2 h, 80% methanol for 2 h, 60% methanol for 2 h, 40% methanol for 2 h, 20% methanol for 2 h and PBS for 2 h. Tissues were permeabilized in PBS/0.2% Triton X-100/0.1% deoxycholate/10% DMSO/25 mM EDTA (pH 6.5) at 37 °C overnight for 24 h and blocked in PBS/0.2% Triton X-100/10% DMSO/5% normal donkey serum/25 mM EDTA at 37 °C for 24 h.

Tissues were incubated with primary antibody, goat anti-VEGFR-3 (R&D Systems, AF743, diluted 1:1,000), in PBS/0.2% Tween-20/10 µg ml^{-1} heparin/5% normal donkey serum/25 mM EDTA (pH 6.5) at 37 °C for 72 h. Tissues were washed in PBS/0.2% Tween-20/10 µg ml^{-1} heparin/25 mM EDTA (pH 6.5) at 37 °C for 24 h, with fresh buffer changed every 6 h. The tissues were further incubated with Alexa Fluor-conjugated secondary antibodies diluted (1:500) in PBS/0.2%Tween-20/10 µg ml^{-1} heparin/5% normal donkey serum/25 mM EDTA (pH 6.5) at 37 °C for 72 h and washed in PBS/0.2% Tween-20/10 µg ml^{-1} heparin/25 mM EDTA (pH 6.5) at 37 °C for 48 h, with fresh buffer changed every 6 h.

For optical-clearing steps, tissues were embedded in PBS/0.8% agarose. The tissue blocks were incubated in a methanol gradient: 20% methanol for 4 h, 40% methanol for 2 h, 60% methanol for 2 h, 80% methanol for 2 h and 100% methanol for 2 h twice at room temperature. Tissue blocks were then incubated in a mixture of dichloromethane and methanol (2:1 (vol:vol)) for 2 h twice, followed by 100% dichloromethane for 30 min four times at room temperature. The tissue blocks were cleared in 100% dibenzyl-ether for 12 h three times at room temperature.

All incubation steps were performed with gentle shaking.

Three-dimensional fluorescence imaging. Optically cleared tissues were imaged on a LaVision Biotec Ultramicroscope II equipped with a sCMOS camera (Andor Neo) and a ×2/0.5-NA objective (MVPLAPO) covered with a 6-mm-working distance dippingcap. Version 144 of the ImSpector Microscope Controller software by LaVision Biotec was supported. Tissue blocks were immersed in the imaging chamber filled with 100% dibenzyl-ether. For imaging at ×1.26 effective magnification, tissues were scanned by three combined lightsheets from the left side with a step size of 4 µm. Image stacks were acquired by the continuous lightsheet scanning method without the contrast-blending algorithm.

Imaris (https://imaris.oxinst.com/packages) was used to reconstruct the image stacks. For display in figures and movies, a gamma correction of 1.3–1.6 was applied to the raw data. Orthogonal 3D projections of the image stacks were generated for the representative images shown in the figures. Movies were produced with a frame rate of 30 fps.

Immunohistochemistry, imaging and quantification. Mice were perfused with ice-cold PBS followed by 4% PFA by puncturing the right auricle. For visualization of MLVs in the whole mount, skin and neck muscles were stripped from the skull, and the mandible and the skull rostral to the maxillae were removed, after which the top of the skull was removed with surgical scissors as previously described[2]. Whole-mount meninges were fixed while still attached to the skull cap in PBS with 4% PFA at 4 °C for 24 h. The dura was then carefully dissected from the skull cap by surgical scissors. For analysis of CLNs, the CLNs were fixed with 4% PFA overnight and dehydrated with a sucrose gradient. Sections (7 µm thick) were sliced using a cryostat (Leica). Whole-mount meninges and sections of CLNs were incubated with blocking solution (PBS containing 3% bovine serum albumin (BSA), 0.5% Triton X-100 and 2% fetal calf serum) for 1 h at room temperature. The blocking step was followed by incubation with appropriate dilutions of primary antibodies, including anti-LYVE-1 (Santa Cruz, sc-65647, 1:300), anti-VEGFR-3 (R&D Systems, AF743, 1:200), anti-PDPN–PE (eBioscience, 53-5381-80, 1:1,000), anti-PROX1 (Angiobio, 11-002, 1:400), anti-ZIKV E protein (BioFrontTech, BF-1176-56, 1:1,000), anti-JEV E protein (GeneTex, GTX125867, 1:500), anti-NeuN (CST, 9664, 1:400), anti-GFAP (CUSABO, CSB_96-100-20C-20, 1:500), anti-VEGF-C (Santa Cruz, sc-374628, 1:100), anti-CD86-APC (Invitrogen,

17-0862-81, 1:500), anti-MHC II–PE (BD Bioscience, 553552, 1:500), anti-CD206–APC (eBioscience, 17-2061-82, 1:500) and anti-CD11b–APC (eBioscience, 17-0112-83, 1:500), in PBS containing 3% BSA and 0.5% Triton X-100 overnight at 4 °C. Meningeal whole mounts were then washed three times for 8 min at room temperature in PBS, followed by incubation with Alexa Fluor 594/647 donkey anti-rat/goat IgG (Invitrogen, A-21209, 1:2,000; Invitrogen, A-21447, 1:1,000) for 1 h at room temperature in PBS containing 3% BSA and 0.5% Triton X-100. Tissue was washed three times for 8 min with PBS after incubating with DAPI (1:1,000) in PBS for 10 min at room temperature and mounted with glass slips and coverslips. Images were acquired by confocal microscopy (Leica TCS SP8 confocal microscope, Nikon A1 confocal microscopy) and a Zeiss Axio Scan Z1. Quantitative analysis was performed using ImageJ, iMaris and Volocity software.

Flow cytometry. Mice were anesthetized with ketamine (100 mg kg^{-1}) and xylazine (10 mg kg^{-1}) in saline by intraperitoneal injection and transcardially perfused with ice-cold PBS. Lymph nodes were then dissected and gently pressed through 70-µm nylon mesh cell strainers with a sterile plastic plunger to obtain a single-cell suspension. Brains were digested with collagenase IV (0.05%; Sigma-Aldrich) and DNAse I (10 µg ml^{-1}; Roche) for 60 min at 37 °C before being strained. Cells were then centrifuged at 300*g* at 25 °C for 10 min. Brain cells were resuspended in 37% Percoll (GE Life Sciences) and centrifuged at 300*g* for 30 min. Cell pellets were washed, resuspended in ice-cold FACS buffer (pH 7.2; PBS, 2 mM EDTA and 0.5% BSA) and were stained for extracellular markers with the following antibodies at a 1:200 dilution: rat anti-CD45–BV421 (103134, BioLegend), rat anti-B220–FITC (11-0452-82, eBioscience), rat anti-MHC II–PE (553552, BD Bioscience), rat anti-MHC II–APC (17-5321-81, Invitrogen), rat anti-CD11b–BV605 (101257, BioLegend), rat anti-F4/80–APC–Cy7 (123118, BioLegend), rat anti-Ly6C–PerCP–Cy5.5 (45-5932-82, eBioscience), rat anti-CD11c–PE–Cy7 (25-0114, eBioscience), rat anti-CD19–PerCP–Cy5.5 (45-0193, eBioscience), rat anti-NK1.1–PE (12-5941-81, eBioscience), rat anti-CD4–PE–Cy7 (25-0041-82, eBioscience), rat anti-CD8–APC–Cy7 (A15386, eBioscience), anti-CD80–PE–Cy5 (15-0801-81, Invitrogen), anti-CD86–APC (17-0862-81, Invitrogen) and rat anti-VEGF-C–PE (sc-37462, Santa Cruz). Cells were incubated at 4 °C for 30 min and washed in ice-cold PBS. Fluorescence data were collected with a BD Flow Cytometer (BD LSR Fortessa) and analyzed using FlowJo software (Tree Star).

Sorting of mLECs. To perform FACS of mLECs, mice were anesthetized with ketamine (100 mg kg^{-1}) and xylazine (10 mg kg^{-1}) in saline by intraperitoneal injection and transcardially perfused with ice-cold PBS. Meninges (dura mater and arachnoid) were carefully removed and digested for 15 min at 37 °C with 0.05% collagenase VIII (Sigma-Aldrich) and 10 µg ml^{-1} DNAse I (Roche) in complete medium (DMEM (Gibco) with 2% FBS (Atlas Biologicals), 1% L-glutamine (Gibco), 1% penicillin/streptomycin (Gibco), 1% sodium pyruvate (Gibco), 1% non-essential amino acid (Gibco) and 1.5% HEPES (Gibco)). The digested meninges were gently pressed with a sterile plastic plunger, and single-cell suspensions were obtained after filtration through a 70-µm nylon mesh cell. Individual samples consisted of cell suspensions pooled from five meninges. Cells were then centrifuged at 280*g* at 4 °C for 10 min and resuspended in ice-cold FACS buffer (pH 7.2; PBS, 2 mM EDTA and 0.5% BSA). Cells were stained for extracellular markers with the following antibodies at a 1:200 dilution: anti-CD45–FITC (103108, BioLegend), anti-CD31–PE (561073, BD Pharmingen) and anti-PDPN–APC–Cy7 (127417, BioLegend). Cells were incubated at 4 °C for 30 min and washed in ice-cold PBS. mLECs were then gated as $CD45^{-}CD31^{+}PDPN^{+}$ using the Aria Sorp (BD Biosciences).

i.c.m. injections. Mice were anesthetized with ketamine (100 mg kg^{-1}) and xylazine (10 mg kg^{-1}) in saline by intraperitoneal injection. The skin of the dorsal neck was shaved and cleaned with iodine and 70% ethanol, and ophthalmic solution was placed on the eyes to prevent drying. After the head of the mouse was secured, a skin incision was made in the neck, and the muscle layers were retracted to expose the cisterna magna. The volume of the desired solution was injected into the cisterna magna compartment by a Hamilton syringe (coupled to a 33-gauge needle). After injecting, the needle was left in place to avoid backflow of CSF for 2 min. The skin was then sutured with nylon sutures, after which the mice were allowed to recover on a heatpad until fully awake. For EB injection and quantification, 5 µl of 10% EB (Sigma, E2129) was injected at a rate of 1 µl min^{-1}. Both sides of the dCLNs were collected 5 min, 15 min and 30 min after EB injection. The dCLNs were then incubated with formamide (30 µl per mg of tissue) in a 60 °C water bath for 24 h, and the optical density values were measured with a microplate reader at a 620-nm wavelength for EB concentration. For VSV–GFP injection, 5 µl of VSV–GFP (2×10^9 p.f.u. ml^{-1}) was injected at a rate of 1 µl min^{-1}. Both sides of the dCLNs were collected 3 h, 6 h and 9 h after injection, and the viral titer of VSV–GFP was measured by plaque assay.

Live mouse imaging. The cervical skin of mice was shaved to prevent attenuation of the fluorescent signal. OVA-647 (5 µl; Invitrogen, O34784, 2 mg ml^{-1} in PBS) was injected into the i.c.m. of mice at a rate of 1 µl min^{-1} or the mice were administered 5 µl of OVA-647 (2 mg ml^{-1} in PBS) intranasally. Fluorescence intensity was measured using an IVIS Lumina Series III preclinical in vivo animal imaging system (PerkinElmer) at various time points (30 min, 60 min, 120 min and 180 min) for 3 h. Results were analyzed using a Living Image 4.7.3 (PerkinElmer). Naive mice were used to adjust settings for eliminating background fluorescence.

Two-photon imaging. Mice were anesthetized with ketamine (100 mg kg^{-1}) and xylazine (10 mg kg^{-1}) in saline by intraperitoneal injection. The skin of the head and neck was shaved and cleaned with iodine and 70% ethanol, and ophthalmic solution was placed on the eyes to prevent drying. A skin incision was surgically made in the parietal skull bone. The skull bone was thinned using an electrical micro drill. Five microliters of QD (Invitrogen) was injected into the i.c.m. of mice at a rate of 1 µl min^{-1}, or the mice were retroorbitally injected with 100 µl of DyLight 488-labeled tomato lectin (Vector Laboratories, 1:1 dilution) to label blood vessels. The heads of mice were fixed on a metal holder to minimize movements during live imaging. In vivo imaging was performed at 60 min after injection every 4 min for a total of 120 min using an Olympus FVMPE-RS upright multiphoton laser-scanning system with an Olympus XL plan N ×25/1.05 WMP ∞/0-0.23/FN/18 dipping objective. QD and DyLight 488 were excited optimally tuned to 920/1,100 nm and 850 nm, respectively. Four-dimensional imaging data were collected by obtaining images from the *x*, *y* and *z* planes over time. The resulting images were analyzed with Imaris software.

Lymphatic vessel ligation. Surgical ligation of the lymph vessels that drain into the dCLNs was performed as described previously[2]. Five-week-old mice were anesthetized with ketamine and xylazine in saline by intraperitoneal injection, the skin of the neck was shaved and cleaned with iodine and 70% ethanol, and ophthalmic solution was placed on the eyes to prevent drying. A 2-cm incision was made in the middle 5 mm superior to the clavicle. The sternocleidomastoid muscles were retracted, and the dCLNs were exposed on each side. The afferent lymphatic vessels anterior to dCLNs on each side were tied off with 10-0 synthetic, non-absorbable nylon sutures. Sham-operated mice were subjected to an incision of the skin and retraction of the sternocleidomastoid muscle but were not ligated. The skin was then sutured by nylon sutures, after which the mice were allowed to recover on a heatpad until fully awake.

Visudyne treatment. Visudyne treatment was performed as previously described[47]. In brief, 5-week old mice were anesthetized with ketamine and xylazine in saline by intraperitoneal injection. Visudyne (5 µl; APExBIO, A8327), reconstituted according to the manufacturer's instructions (2 mg ml^{-1}), was injected into the cisterna magna at a rate of 1 µl min^{-1}. After 15 min, Visudyne was photoconverted with a non-thermal 689-nm wavelength laser light (Changchun Laser Technology), with a dose of 50 J cm^{-2} and intensity of 600 mW cm^{-2}, on five different spots through the intact skull (the injection site, left and right TS, the SSS and the junction of all sinuses), and each spot was irradiated for 83 s. For control mice, the vehicle instead of Visudyne was injected into the cisterna magna, and other treatments were the same as the Visudyne group. The skin was then sutured by nylon sutures, after which the mice were allowed to recover on a heatpad until fully awake.

Transcranial recombinant VEGF-C delivery. VEGF-C delivery was achieved as previously described[6]. In brief, a hydrogel of 1.4% hyaluronic acid and 3% methylcellulose alone (vehicle) or with 200 ng ml^{-1} of encapsulated human VEGF-C (PeproTech) was prepared. Sterile methylcellulose (4,000 cP, Sigma-Aldrich) and hyaluronic acid (1,500–1,800 kDa, Sigma-Aldrich) were sequentially dissolved in sterile 0.1 M PBS at 4 °C overnight. Lyophilized VEGF-C was resuspended as particulate at 100 µg ml^{-1} in sterile water, and the solution was diluted to 2,000 ng ml^{-1} with 0.5% sterile methylcellulose in PBS. The particulate solution, or vehicle (0.5% methylcellulose), was mixed into the hydrogel presolution at 1:10 and loaded into a syringe for gelation at 37 °C. Hydrogels were prepared on the day of the experiment and kept warm inside the individual syringes until applied onto the skull of the mouse. The mouse was anesthetized by intraperitoneal injection of anesthetic, and the head was secured. An incision was made in the scalp skin, and the skull was thinned at the junction of all sinuses and above the TS. One hundred microliters of each hydrogel solution was delivered from the syringe into the thinned skull surface. The scalp skin was then sutured on top of the solidified hydrogel, and the mice were allowed to recover on a heatpad until fully awake. After 14 d, 200 ng ml^{-1} VEGF-C in sterile PBS was subcutaneously injected into the thinned skull three times, one injection every other day.

Statistical analysis. No statistical methods were used to predetermine sample sizes, but our sample sizes are similar to those reported in previous publications[6–8]. Animals from different cages, but within the same experimental group, were selected to assure randomization. Experimenters were blinded to the identity of experimental groups. Any animals or data points were not excluded from the analyses. Data distribution was assumed to be normal, but this was not formally tested. Statistical data analysis was performed with GraphPad Prism 7.0 software. For detailed statistical information, please see Supplementary Table 2. Statistical significance was determined by a two-tailed unpaired Student's *t*-test between two groups, one-way ANOVA with a multiple comparisons test or two-way ANOVA

with a multiple comparisons test. A P value of <0.05 was considered statistically significant ($^{*}P<0.05$, $^{**}P<0.01$, $^{***}P<0.001$ and $^{****}P<0.0001$).

Reporting Summary. Further information on research design is available in the Nature Research Reporting Summary linked to this article.

Data availability

The data that support the findings of this study are available in this manuscript and the Supplementary Information. Source data are provided with this paper.

Code availability

Customized code or algorithms were not used to generate results in the present study.

References

46. Shen, T., Liu, K., Miao, D. N., Cao, R. B. & Chen, P. Y. Effective inhibition of Japanese encephalitis virus replication by shRNAs targeting various viral genes in vitro and in vivo. *Virology* **454**, 48–59 (2014).
47. Chen, J. M. et al. Meningeal lymphatics clear erythrocytes that arise from subarachnoid hemorrhage. *Nat. Commun.* **11**, 3159 (2020).

Acknowledgements

This work was supported by grants from the National Natural Science Foundation of China (81630043 to B.W., 81825011 to H.W., 81930038 to H.W. and 81961160738 to B.W.), the Ministry of Science and Technology of China (2018YFA0800702 to H.W.), the Strategic Priority Research Program of the Chinese Academy of Sciences (XDB19030200 to H.W.), Shanghai Municipal Science and Technology Major Project and Key National Science and Technology Programs in Shanghai (218014204 to B.W.). We thank the Core Facility and Technical Support in the Shanghai University and Wuhan Institute of Virology, CAS. We thank the Core Facility of Molecular Biology and Core Facility of Cell Biology in the Shanghai Institute of Biochemistry and Cell Biology for their technical support and help. We thank C. Gu of Huazhong Agricultural University for providing anti-JEV E. We thank M. Jin of Huazhong Agricultural University for providing VSV–GFP. We thank the laboratory of Z. Qian of Institute Pasteur of Shanghai, CAS, for providing HSV-1. We thank the laboratory of H. Wang of the Wuhan Institute of Virology, CAS, for providing ZIKV. We thank Q. Leng of the Institute Pasteur of Shanghai, CAS, for providing IFN receptor-deficient mice. We thank Q. Liang of Shanghai University of Traditional Chinese Medicine for providing the non-thermal 689-nm laser. We thank S. Cao of Huazhong Agricultural University for providing the BHK-21 cell line. We thank H. Wang of Shanghai Institute of Biochemistry and Cell Biology, CAS, for providing the 293T cell line. We thank H. Yan of Wuhan Institute of Virology, CAS, for providing the C6/36 cell line.

Author contributions

X.L. and L.Q. performed most of the experiments and statistical analysis. D.Y. performed the two-photon imaging. F.Z. and S.H. performed hLECs experiments. S.H. and X.Z. participated in animal experiments. Y.S. performed volume fluorescence imaging. C.C. performed RABV infection. B.W. and H.W. conceptualized and designed experiments. J. Ye., L.Z., J. Yang and S.C. helped with technical support. X.L., L.Q., B.W., D.M.A. and H.W. wrote the paper. All authors approved the final version of the manuscript.

Competing interests

The authors declare no competing interest.

Additional information

Extended data is available for this paper at https://doi.org/10.1038/s41593-022-01063-z.

Supplementary information The online version contains supplementary material available at https://doi.org/10.1038/s41593-022-01063-z.

Correspondence and requests for materials should be addressed to Hongyan Wang or Bin Wei.

Peer review information *Nature Neuroscience* thanks Robyn Klein and the other, anonymous, reviewer(s) for their contribution to the peer review of this work.

Reprints and permissions information is available at www.nature.com/reprints.

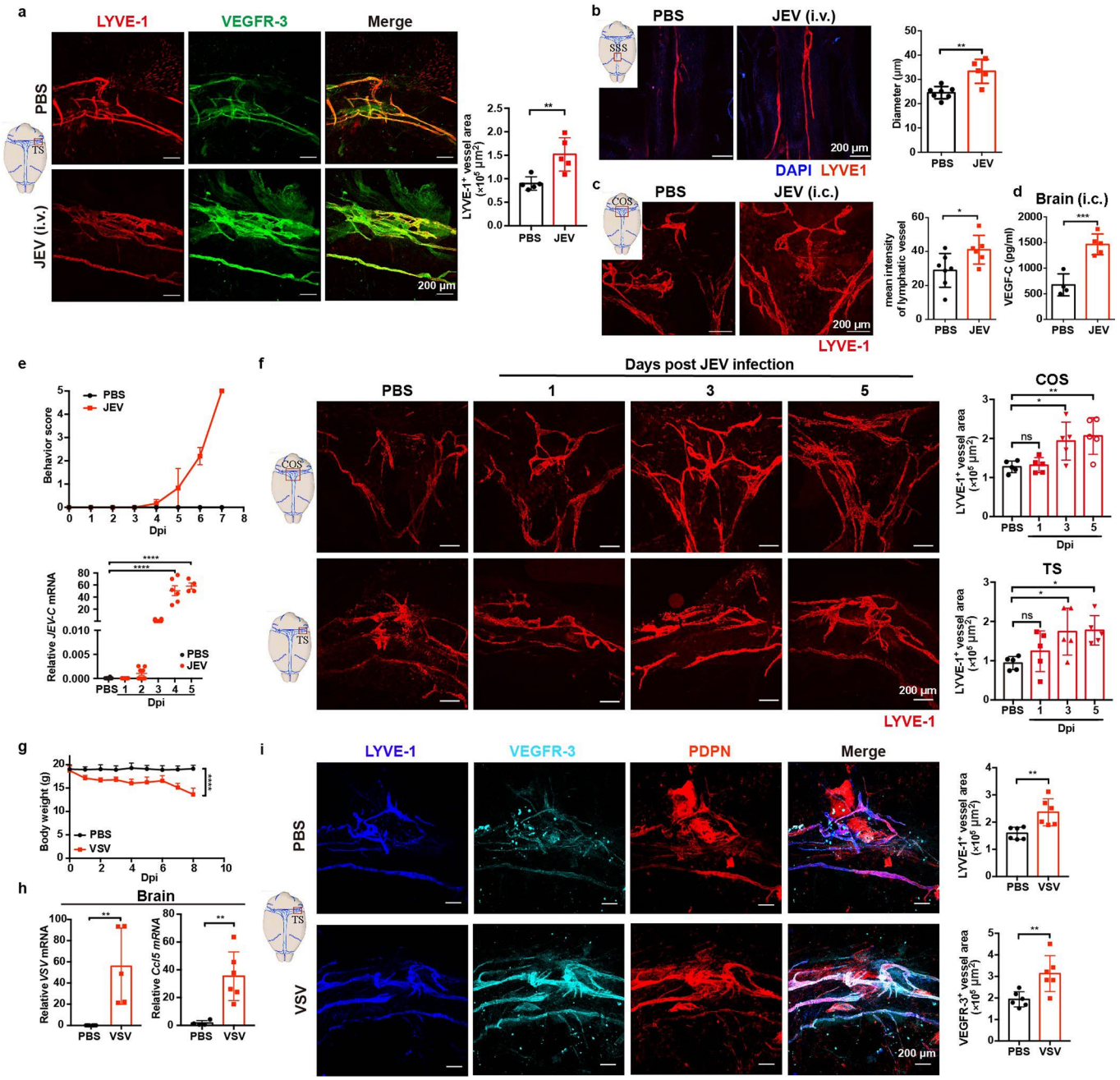

Extended Data Fig. 1 | JEV and VSV infections induce dorsal meningeal lymphangiogenesis. (**a-f**). C57BL/6 mice were intravenously (i.v.) or intracerebrally (i.c.) infected with JEV or PBS. **a**. Representative images of LYVE-1 and VEGFR-3 staining and quantification of the area of LYVE-1$^+$ MLVs in TS at 7 Dpi (n = 5). **b**. Representative image and quantification of the diameter of LYVE-1$^+$ MLVs along the SSS in JEV (i.v.) infected mice (n = 7 PBS; n = 5 JEV). **c**. Representative images and quantification of the mean intensity of LYVE-1$^+$ MLVs in COS after JEV (i.c.) infection (n = 7 PBS; n = 6 JEV). **d**. VEGF-C concentrations in the brain after JEV (i.c.) injection (n = 4 PBS; n = 5 JEV). **e**. The daily behavior scores of mice (n = 6) and the relative mRNA levels of JEV-C gene (n = 8 PBS; n = 4-8 JEV) in the brain at different time points after JEV (i.v.) infection. **f**. Representative images and quantification of the area of LYVE-1 staining in COS and TS at day 1, day 3 and day 5 after JEV (i.v.) injection (n = 5). (**g-i**). C57BL/6 mice were intranasally infected with VSV. **g**. The daily body weight of mice after VSV infection (n = 6). **h**. The relative mRNA levels of VSV (n = 6 PBS; n = 5 JEV) and *Ccl5* (n = 4 PBS; n = 6 JEV) in the brain at 8 Dpi. **i**. Representative images and the quantification of meningeal LYVE-1, VEGFR-3, PDPN staining in the TS at 8 Dpi (n = 6). Data are presented as Mean ± SD. ns, not significant ($p > 0.05$), *$p < 0.05$, **$p < 0.01$, ***$p < 0.001$ and ****$p < 0.0001$, two-tailed, unpaired Student's *t* test (a right, b right, c right, d, g, h and i right), one-way ANOVA with Holm-Sidak's multiple comparisons test (e and f right). Data from at least 3 independent experiments. Detailed statistical information is shown in Supplementary Table 2.

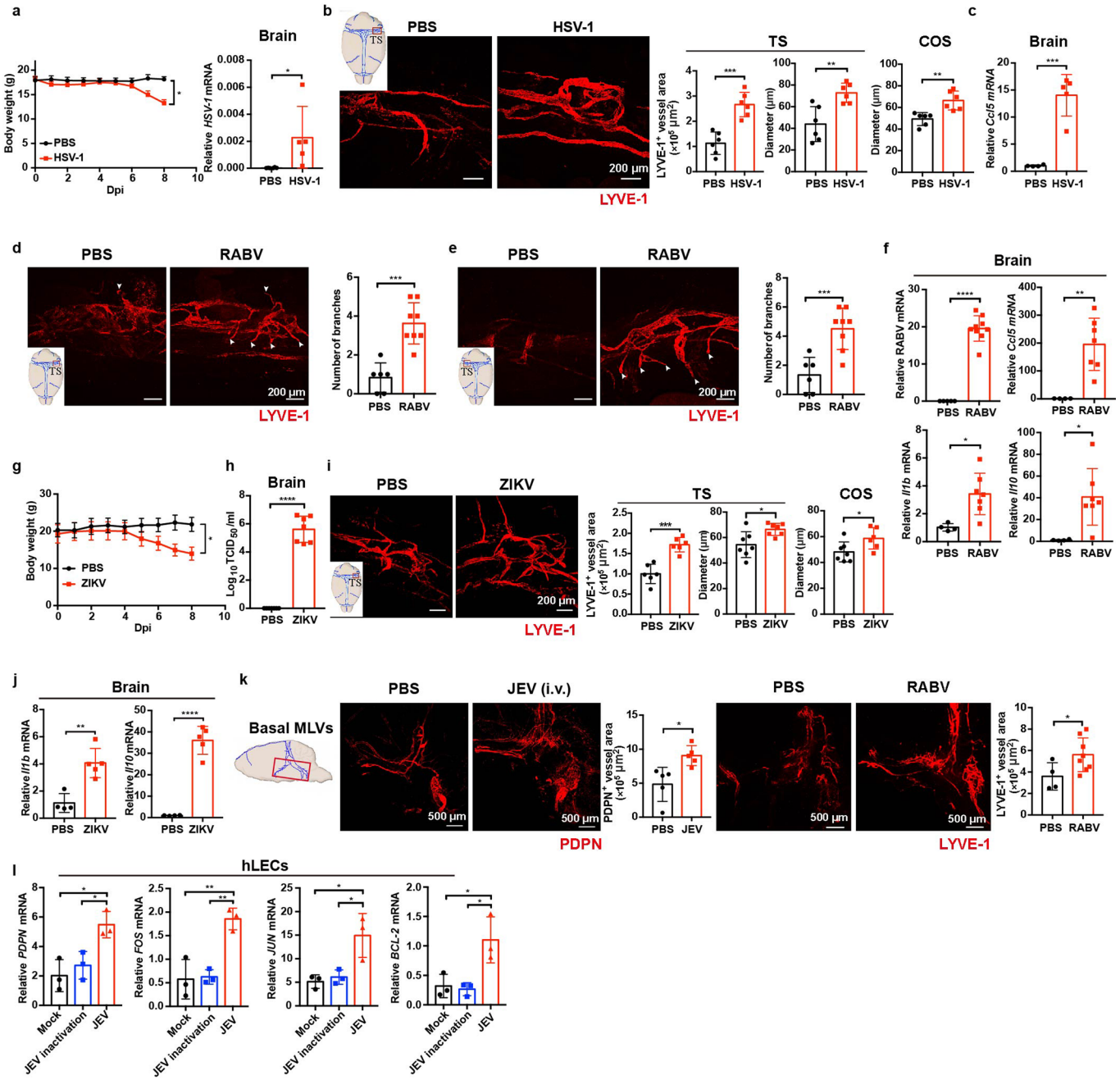

Extended Data Fig. 2 | HSV-1, ZIKV and RABV infections induce dorsal meningeal lymphangiogenesis. (**a-c**). Mice were corneally infected with HSV-1. **a**. Left, the daily body weight of mice (n = 7 PBS; n = 6 HSV-1). Right, mRNA levels of HSV-1 in the brain at 8 Dpi (n = 6 PBS; n = 5 HSV-1). **b**. Representative meningeal LYVE-1 staining and quantification of the area and diameter of LYVE-1$^+$ MLVs in COS or TS (n = 6). **c**. mRNA levels of *Ccl5* in the brain (n = 4 PBS; n = 5 HSV-1). (**d-f**). Mice were intramuscularly infected with RABV. Representative meningeal LYVE-1 staining (d left, e left) and quantification of lymphatic branches (white arrowheads) (d right, e right) in TS (n = 6 PBS; n = 8 RABV). **f**. mRNA levels of RABV (n = 5 PBS; n = 9 RABV), *Ccl5*, *Il1b* and *Il10* (n = 4 PBS; n = 7 RABV) in the brain at 8 Dpi. (**g-j**). AG6 mice were intraperitoneally infected with ZIKV. g. The daily body weight of mice (n = 5 PBS; n = 8 ZIKV). **h**. Viral titers were detected in the brain at 8 Dpi (n = 7). i. Representative images and quantification of the area and diameter of LYVE-1$^+$ MLVs in COS or TS (n = 6 or 7 PBS; n = 6 or 7 ZIKV). **j**. mRNA levels of *Il1b* and *Il10* in the brain at 8 dpi (n = 4 PBS; n = 5 ZIKV). **k**. Mice were intravenously infected with JEV or intramuscularly infected with RABV. Representative images and quantification of PDPN$^+$ basal MLVs of JEV-infected mice at 7 dpi (n = 5). Representative images and quantification of LYVE-1$^+$ basal MLVs of RABV-infected mice at 8 dpi (n = 4 PBS; n = 8 RABV). **l**. mRNA levels of *PDPN*, *FOS*, *JUN* and *BCL-2* in hLECs treated with 0.1 MOI JEV, inactivated JEV or untreated for 72 h (n = 3). Data are presented as Mean ± SD. not significant ($p > 0.05$), *$p < 0.05$, **$p < 0.01$, ***$p < 0.001$ and ****$p < 0.0001$, a two-tailed, unpaired Student's *t* test (a, b right, c, d right, e right, f, g, h, i right, j, k), one-way ANOVA with Holm-Sidak's multiple comparisons test (l). Data from at least 2 independent experiments. Detailed statistical information is shown in Supplementary Table 2.

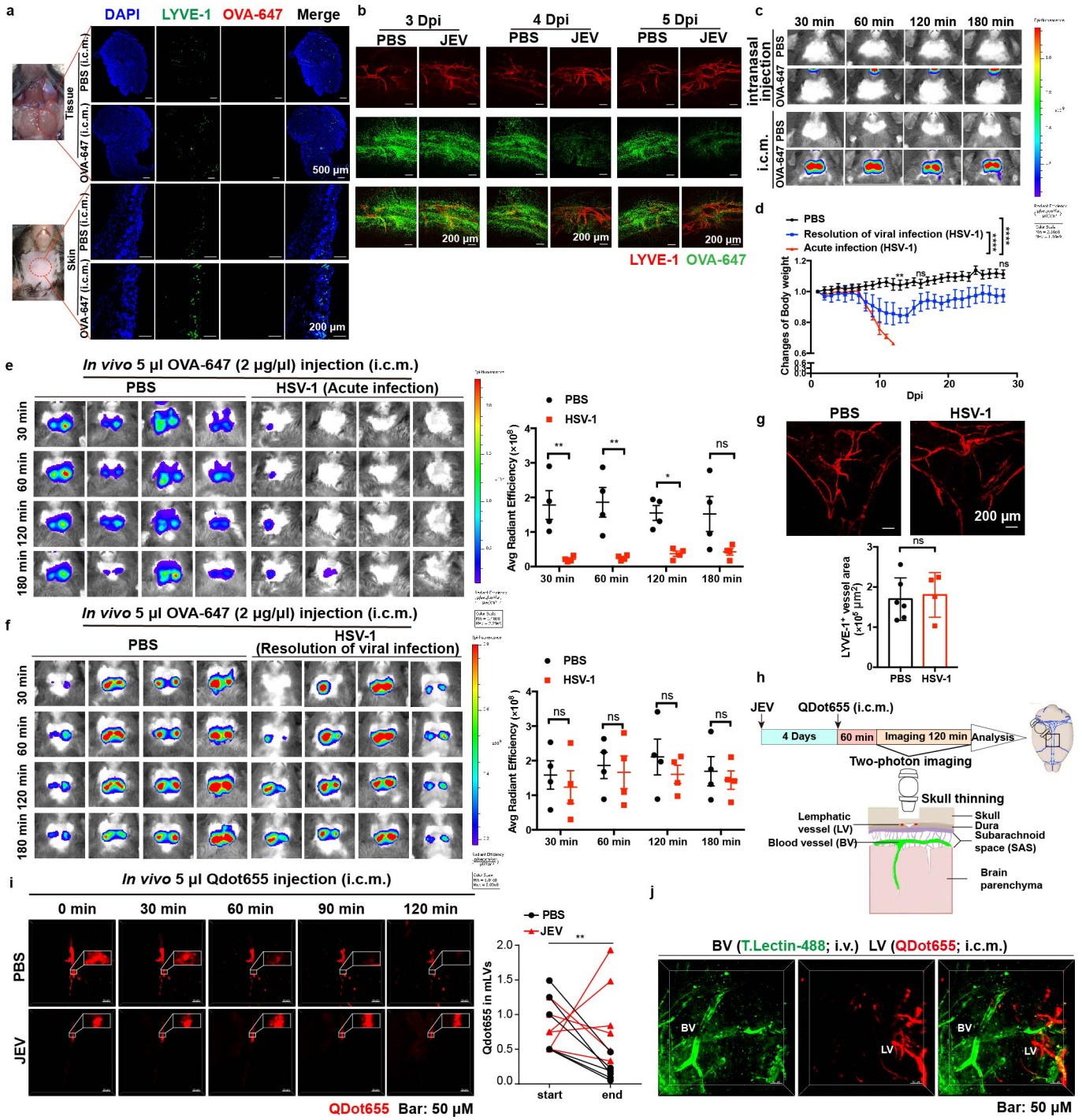

Extended Data Fig. 3 | MLVs function to drain biological molecules upon virus infection. a. Representative images of LYVE-1 staining and OVA-647 in tissue around sCLN and the superficial skin of neck at 180 min after i.c.m. injection of OVA-647. **b**. Representative images of LYVE-1 staining and OVA-647 in TS of meninges after i.c.m. injection of OVA-647 (2 μg/μl) at 3, 4, and 5 Dpi of JEV. **c**. The ventral images show the biodistribution of OVA-647 in the mice at the indicated time points after i.c.m. or intranasally injection with OVA-647. (**d-f**). Mice were corneally infected with HSV-1. **d**. The daily body weight of mice in PBS group (n = 5), the acute infection group (n = 6;) and the resolution of viral infection group (n = 4). (**e, f**). The ventral images show the biodistribution of OVA-647 and the retention of OVA-647 in cervical region was quantified at 10 days (**e**) or 28 days (**f**) (n = 4). **g**. Representative images of LYVE-1 staining and quantification of the area of LYVE-1⁺ MLVs in COS at 28 Dpi (n = 6 PBS; n = 4 HSV-1). (**h-j**). C57BL/6 mice were (i.v.) infected with JEV or PBS. 5 μl QDot655 was injected in i.c.m. of JEV or PBS-injected mice at 4 Dpi. Change of QDot655 in MLVs was monitored through a thinned skull preparation by multiphoton microscopy system. **h**. Schematic of QDot655 treatment. **i**. Representative images and the quantification of Qdot655 in MLVs were captured at different timepoints (n = 6). See also video S3. **j**. Representative images of Qdot655 and Lectin-488 (labeled blood vessel) were captured by multiphoton microscopy system. See also video S4. The data are presented as Mean ± SEM (d, e, f) or as Mean ± SD (g). ns, not significant ($p > 0.05$), $^{**}p < 0.01$ and $^{****}p < 0.0001$, a two-tailed, unpaired Student's *t* test (g), one-way ANOVA with Holm- Sidak's multiple comparisons test (d) and two-way ANOVA with Holm- Sidak's multiple comparisons test (e right, f right, i). Detailed statistical information is shown in Supplementary Table 2.

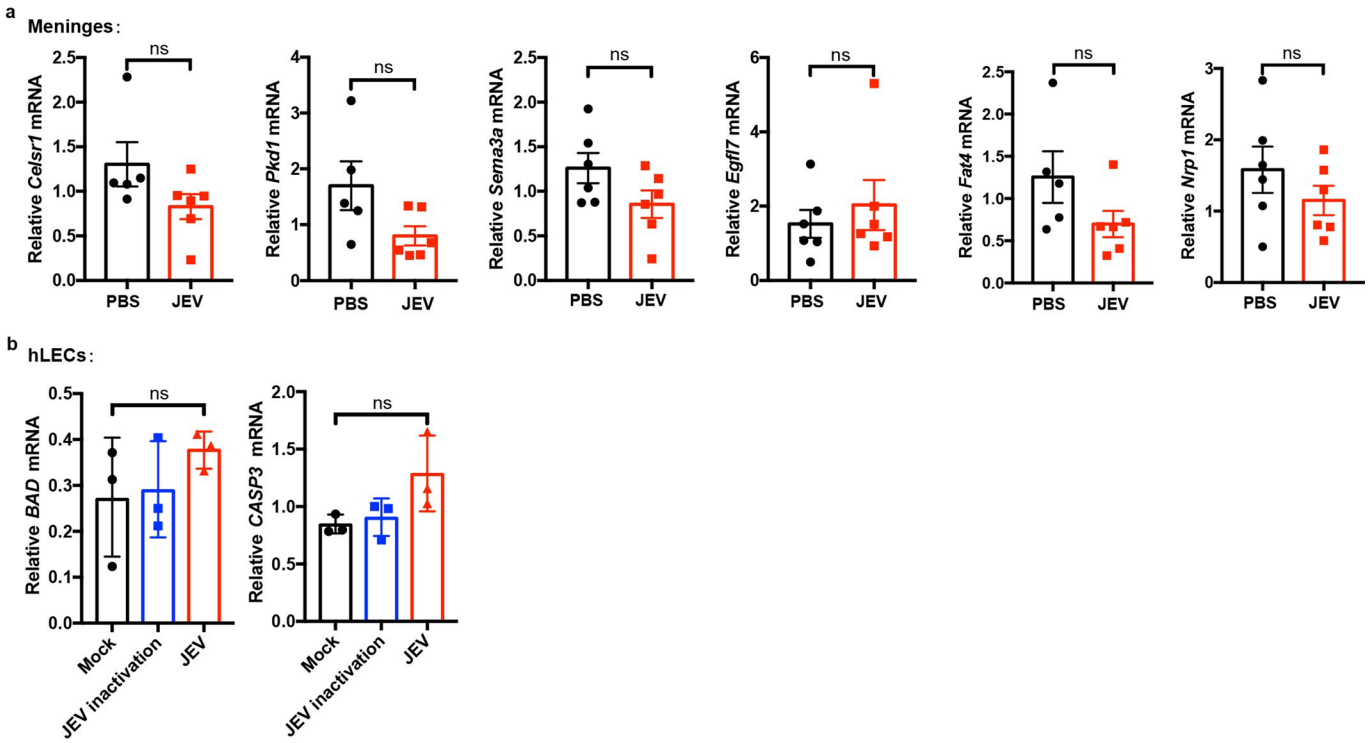

Extended Data Fig. 4 | The expression of genes that regulated cell polarization of LECs. a. The relative mRNA levels of *Celsr1*, *Pkd1*, *Sema3a*, *Egfl7*, *Fat4*, *Nrp1* in meninges of JEV (n = 6) or PBS (n = 5 or 6) injected mice. The data are presented as Mean ± SEM. **b**. hLECs treated with 0.1 MOI JEV, inactivated JEV or untreated for 72 h. The relative mRNA levels of *BAD* and *CASP9* in hLECs (n = 3). The data are presented as Mean ± SD. ns, not significant ($p > 0.05$), a two-tailed, unpaired Student's *t* test (a) and one-way ANOVA with Holm- Sidak's multiple comparisons test (b). Detailed statistical information is shown in Supplementary Table 2.

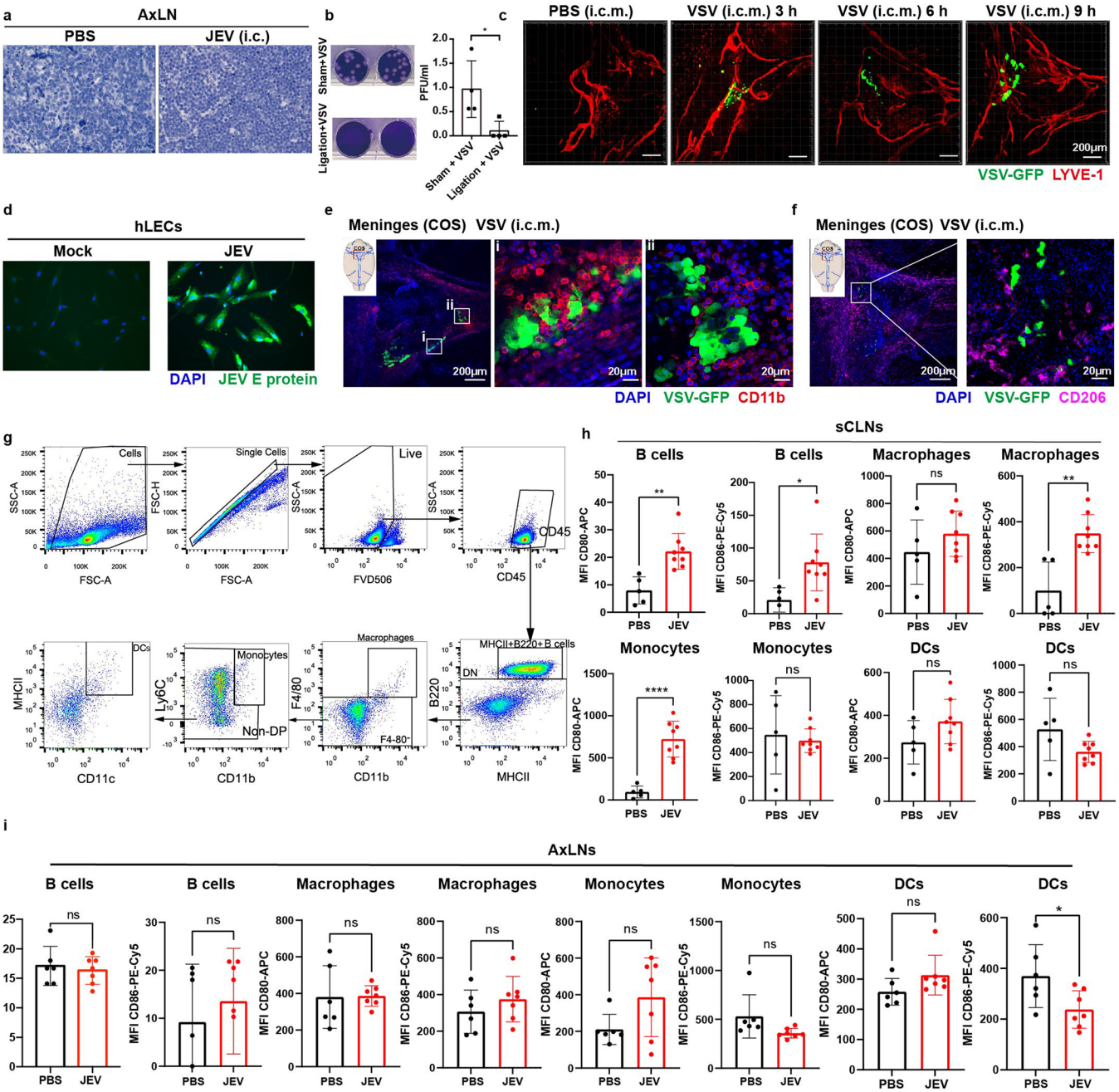

Extended Data Fig. 5 | Meningeal lymphatic vessels drain neurotropic viral particles from CNS to CLNs. a. Immunohistochemical analysis of JEV E protein in AxLN sections in JEV or PBS (i.c.) injected mice with severe JE cases. **b**. 5-week-old C57BL/6 mice were ligation of dCLVs, and 7 days later, VSV-GFP was i.c.m. injected. The viral titers of VSV-GFP in dCLNs were measured by plaque assay after 3 h injection (n = 4). **c**. Representative images of the colocalization of VSV-GFP (green) and LYVE-1$^+$ MLVs in TS and COS at 3 h, 6 h, 9 h after i.c.m. injection of VSV-GFP. **d**. Representative images of JEV E protein staining in hLECs treated with 1 MOI JEV for 48 h. (**e, f**). VSV-GFP was injected in i.c.m. of C57BL/6 mice. **e**. Representative images of DAPI, VSV-GFP, CD11b staining in COS of meninges at 9 h after VSV-GFP injection. **f**. Representative images of DAPI, VSV-GFP, CD206 staining in COS of meninges at 9 h after VSV-GFP injection. (**g-i**). FACS analysis of the CD45$^+$ cells, macrophages, monocytes and DCs in sCLNs and AxLNs of mice (i.c.) injected with JEV and PBS. **g**. Gating strategy employed to identify CD45$^+$ cells, B cells (MHC II$^+$ B220$^+$), macrophages (F4/80$^+$ CD11b$^+$), monocytes (F4/80$^-$ Ly6c$^+$ CD11b$^+$) and DCs (CD11C$^+$ MHC II$^+$). (**h, i**). MFI of CD86 and CD80 in B cells, macrophages, DCs or monocytes in sCLNs (n = 5 PBS; n = 8 JEV) or AxLNs (n = 6 PBS; n = 7 JEV) of JEV-infected mice. Data are presented as mean ± SD. not significant ($p > 0.05$), *$p < 0.05$, **$p < 0.01$, a two-tailed, unpaired Student's t test (b right, h and i). Data from at least 2 independent experiments. Detailed statistical information is shown in Supplementary Table 2.

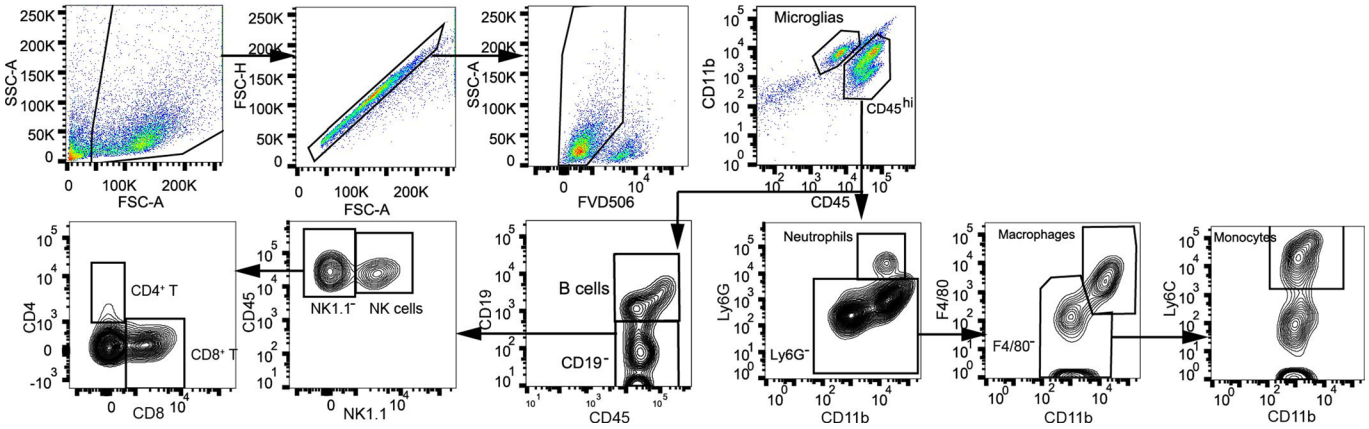

Extended Data Fig. 6 | Gating strategy of cells in brain of JEV-infected mice. The gating strategy of CD45$^+$ cells, neutrophils, macrophages, monocytes, CD8$^+$ T cells, CD4$^+$ T cells, NK cells, microglia and B cells in the brain of JEV-infected mice.

nature portfolio

Corresponding author(s): Dr Hongyan Wang and Dr. Bin Wei

Last updated by author(s): Dec 22, 2021

Reporting Summary

Nature Portfolio wishes to improve the reproducibility of the work that we publish. This form provides structure for consistency and transparency in reporting. For further information on Nature Portfolio policies, see our Editorial Policies and the Editorial Policy Checklist.

Statistics

For all statistical analyses, confirm that the following items are present in the figure legend, table legend, main text, or Methods section.

n/a	Confirmed	
☐	☒	The exact sample size (*n*) for each experimental group/condition, given as a discrete number and unit of measurement
☐	☒	A statement on whether measurements were taken from distinct samples or whether the same sample was measured repeatedly
☐	☒	The statistical test(s) used AND whether they are one- or two-sided *Only common tests should be described solely by name; describe more complex techniques in the Methods section.*
☐	☒	A description of all covariates tested
☐	☒	A description of any assumptions or corrections, such as tests of normality and adjustment for multiple comparisons
☐	☒	A full description of the statistical parameters including central tendency (e.g. means) or other basic estimates (e.g. regression coefficient) AND variation (e.g. standard deviation) or associated estimates of uncertainty (e.g. confidence intervals)
☐	☒	For null hypothesis testing, the test statistic (e.g. *F*, *t*, *r*) with confidence intervals, effect sizes, degrees of freedom and *P* value noted *Give P values as exact values whenever suitable.*
☒	☐	For Bayesian analysis, information on the choice of priors and Markov chain Monte Carlo settings
☐	☒	For hierarchical and complex designs, identification of the appropriate level for tests and full reporting of outcomes
☒	☐	Estimates of effect sizes (e.g. Cohen's *d*, Pearson's *r*), indicating how they were calculated

Our web collection on statistics for biologists contains articles on many of the points above.

Software and code

Policy information about availability of computer code

Data collection	LaVision Biotec Ultramicroscope II equipped with the sCMOS camera, leica TCS SP8 Confocal Microscope, Nikon A1 confocal microscopy, Zeiss Axio Scan Z1, Living Image 4.7.3, Olympus FVMPE-RS upright multiphoton laser-scanning system, BD Flow Cytometer (BD LSRFortessa), Aria Sorp (BD Biosciencess), ImSpector Microscope Controller software.
Data analysis	Graphpad Prism7 software, Image J 1.52v, iMaris x64 9.5.1, volocity software 6.1.1, Living Image 4.7.3, FlowJo software 10.4

For manuscripts utilizing custom algorithms or software that are central to the research but not yet described in published literature, software must be made available to editors and reviewers. We strongly encourage code deposition in a community repository (e.g. GitHub). See the Nature Portfolio guidelines for submitting code & software for further information.

Data

Policy information about availability of data

All manuscripts must include a data availability statement. This statement should provide the following information, where applicable:

- Accession codes, unique identifiers, or web links for publicly available datasets
- A description of any restrictions on data availability
- For clinical datasets or third party data, please ensure that the statement adheres to our policy

We will provide the raw data upon request.

Field-specific reporting

Please select the one below that is the best fit for your research. If you are not sure, read the appropriate sections before making your selection.

☒ Life sciences ☐ Behavioural & social sciences ☐ Ecological, evolutionary & environmental sciences

For a reference copy of the document with all sections, see nature.com/documents/nr-reporting-summary-flat.pdf

Life sciences study design

All studies must disclose on these points even when the disclosure is negative.

Sample size	The sample size chosen for our animal experiments and immunofluorescence staining assay in this study were estimated based on the similar experiments published in Nature neuroscience 2018 (DOI: 10.1016/j.vetmic.2019.108430), Nature 2020 (DOI: 10.1038/s41593-018-0227-9) and Nature communications 2020 (DOI: 10.1038/s41467-020-16851-z).
Data exclusions	No data were excluded.
Replication	We at least independently repeated three or more than three of all the data. all attempts at replication were successful.
Randomization	All animal- and cell- based samples in each group were included.
Blinding	Samples were randomly allocated to different experimental groups

Reporting for specific materials, systems and methods

We require information from authors about some types of materials, experimental systems and methods used in many studies. Here, indicate whether each material, system or method listed is relevant to your study. If you are not sure if a list item applies to your research, read the appropriate section before selecting a response.

Materials & experimental systems

n/a	Involved in the study
☐	☒ Antibodies
☐	☒ Eukaryotic cell lines
☒	☐ Palaeontology and archaeology
☐	☒ Animals and other organisms
☒	☐ Human research participants
☒	☐ Clinical data
☒	☐ Dual use research of concern

Methods

n/a	Involved in the study
☒	☐ ChIP-seq
☐	☒ Flow cytometry
☒	☐ MRI-based neuroimaging

Antibodies

Antibodies used	goat anti-VEGFR3 (R&D Systems, Cat#AF743, LotDAB0320021), anti-LYVE-1 (Santa Cruz, sc-65647,Lot#L2917), anti-PROX1 (Angiobio; 11-002), anti-PDPN-PE (eBioscience; 53-5381-80), anti-ZIKV E protein (BioFrontTech; BF-1176-56), anti-JEV E protein (GeneTex; GTX125867), anti-NeuN (CST; 9664), anti-GFAP (CUSABO; CSB_96-100-20C-20), anti-VEGF-C (santa Cruz; sc-374628), anti-CD86-APC (Invitrogen; 17-0862-81), anti-MHC II-PE (BD Bioscience; 553552), anti-CD206-APC (eBioscience; 17-2061-82), anti-CD11b-APC (eBioscience; 17-0112-83), rat anti-CD45–BV421 (103134, Biolegend), rat anti-B220–FITC (11-0452-82, eBioscience), rat anti-MHC II–PE (553552, BD Bioscience), rat anti-MHC II–APC (17-5321-81, Invitrogen), rat anti-CD11b–BV605(101257, BioLegend), rat anti-F4/80–APC–Cy7 (123118, Biolegend), rat anti-Ly6C–PerCP–Cy5.5 (45-5932-82, eBioscience), rat anti-CD11c–PE-Cy7 (25-0114, eBioscience), rat anti-CD19–PerCP–Cy5.5 (45-0193, eBioscience), rat anti-NK1.1–PE (12-5941-81, eBioscience), rat anti-CD4–PE-Cy7 (25-0041-82, eBioscience), rat anti-CD8–APC-Cy7 (A15386, eBioscience), anti-CD80–PE-Cy5 (15-0801-81, Invitrogen),
Validation	The anti-JEV E antibody for IHC provided by Huazhong Agricultural University was validated on the experiments published in 2019 (DOI: 10.1016/j.vetmic.2019.108430). Each antibody was validated for the species (mouse) and application (immunohistochemistry or flow cytometry/cell sorting) by the correspondent manufacturer. The usage was described in the methods section of the manuscript: immunohistochemistry: Whole mounts meninges and sections of CLNs were incubated with blocking solution (PBS containing 3% BSA, 0.5% Triton-X-100 and 2% fetal calf serum) for 1 h at room temperature. The blocking step was followed by incubation with appropriate dilutions of primary antibodies: anti-LYVE-1 (Santa Cruz, sc-65647, 1:300), anti-VEGFR-3 (R&D Systems, AF743, 1:200), anti-PDPN-PE (eBioscience; 53-5381-80; 1:1000), anti-PROX1 (Angiobio; 11-002; 1:400), anti-ZIKV E protein (BioFrontTech; BF-1176-56, 1:1000), anti-JEV E protein (GeneTex; GTX125867; 1:500), anti-NeuN (CST; 9664; 1:400), anti-GFAP (CUSABO; CSB_96-100-20C-20; 1:500), anti-VEGF-C (santa Cruz; sc-374628; 1:100), anti-CD86-APC (Invitrogen; 17-0862-81; 1:500), anti-MHC II-PE (BD Bioscience; 553552; 1:500), anti-CD206-APC (eBioscience; 17-2061-82; 1:500), anti-CD11b-APC (eBioscience; 17-0112-83; 1:500) in PBS containing 3% BSA and 0.5% Triton-X-100 overnight at 4 °C. Meningeal whole mounts were then washed three times for 8 min at room temperature in PBS, followed by incubation with Alexa-fluor 594/647 donkey anti rat/goat IgG antibodies

(Invitrogen, A-21209, 1:2000; Invitrogen, A-21447, 1:1000) for 1 h at room temperature in PBS containing 3% BSA and 0.5% Triton-X-100. Tissue was washed 3 times for 8 min with PBS after incubating with DAPI (1:1000) in PBS for 10 min at room temperature, and mounted with glass slips and coverslips.
Flow cytometry: The lymph nodes were then dissected and gently pressed through 70-μm nylon mesh cell strainers with a sterile plastic plunger to obtain a single-cell suspension. The brain was digested with collagenase IV (0.05%; Sigma Aldrich) and DNAse I (10 μg/mL; Roche) for 60 min at 37 °C before being strained. Cells were then centrifuged at 300g at 25 °C for 10 min. Brain cells were resuspended in 37% Percoll (GE Life Sciences) and centrifuged at 300g for 30 min. The cell pellets were washed, resuspended in ice-cold fluorescence-activated cell sorting FACS buffer (pH 7.2; PBS; 2 mM EDTA and 0.5% BSA) and were stained for extracellular markers with the following antibodies at a 1:200 dilution: rat anti-CD45–BV421 (103134, Biolegend), rat anti-B220–FITC (11-0452-82, eBioscience), rat anti-MHC II–PE (553552, BD Bioscience), rat anti-MHC II–APC (17-5321-81, Invitrogen), rat anti-CD11b–BV605(101257, BioLegend), rat anti-F4/80–APC–Cy7 (123118, Biolegend), rat anti-Ly6C–PerCP–Cy5.5 (45-5932-82, eBioscience), rat anti-CD11c–PE-Cy7 (25-0114, eBioscience), rat anti-CD19–PerCP–Cy5.5 (45-0193, eBioscience), rat anti-NK1.1–PE (12-5941-81, eBioscience), rat anti-CD4–PE-Cy7 (25-0041-82, eBioscience), rat anti-CD8–APC-Cy7 (A15386, eBioscience), anti-CD80–PE-Cy5 (15-0801-81, Invitrogen), anti-CD86–APC (17-0862-81, Invitrogen), rat anti-VEGF-C-PE (sc-37462, Santa Cruz). Cells were incubated at 4 °C for 30 min, and then washed in ice-cold PBS.

Eukaryotic cell lines

Policy information about cell lines

Cell line source(s)	BHK-21 cells line was provided by Prof. Shengbo Cao of Huazhong Agricultural University , 293T cells lines was provided by Prof. Hongyan Wang of Shanghai Institute of Biochemistry and Cell Biology. C6/36 cells lines were provided by Dr. Huimin Yan of Wuhan Institute of virology. VERO-E6 were obtained from National collection of Authenticated Cell Cultures (catalog GNO17). Human lymphatic endothelial cells (hLECs) were obtained from ScienCell (catalog #2500). The detailed information were provided in the method section "cells and viruses"
Authentication	the Human lymphatic endothelial cells (hLECs) was validated by the correspondent manufacturer
Mycoplasma contamination	hLECs, BHK-21, VERO-E6, C6/36, 293T cell lines were tested negative for mycoplasma contamination
Commonly misidentified lines (See ICLAC register)	No commonly misidentified cell lines were used.

Animals and other organisms

Policy information about studies involving animals; ARRIVE guidelines recommended for reporting animal research

Laboratory animals	The studies used 5-8-week-old male and female C57BL/6J mice. The experiments (ZIKV-infection) were used the 5-week-old IFN-α/β receptor (IFNAR)-knockout (AG6) mice of both sexes. Specific pathogen-free (SPF) C57BL/6J adult mice of both sexes were purchased from Beijing Vital River Laboratory Animal Technology Co., Ltd. (Beijing, China). AG6 mice with the strain 129 background have been backcrossed onto the C57BL/6 background for more than six generations and were the kind gifted of Dr. Qibin Leng of Institute Pasteur of Shanghai, Chinese Academy of Science. All mice were fed with free access to a standard diet and water and on a 12-h light/dark cycle in rooms maintained at 68 °F and 55% humidity.
Wild animals	no wild animals were used in the study.
Field-collected samples	no field collected samples were used in the study.
Ethics oversight	The animal experiments (JEV, ZIKV, VSV, HSV-1-infection)described in the study were pre-approved by the Ethical Committee for Animal Experiments of Wuhan institute of virology (Protocol No. WIVA39201602, WIVA39201603, WIVA39201803, WIVA39201804); The animal experiments (RABV-infection) described in the study were pre-approved by the Scientific Ethics Committee of Huazhong Agricultural University (permit number HZAUMO-2016-052).

Note that full information on the approval of the study protocol must also be provided in the manuscript.

Flow Cytometry

Plots

Confirm that:

☐ The axis labels state the marker and fluorochrome used (e.g. CD4-FITC).

☒ The axis scales are clearly visible. Include numbers along axes only for bottom left plot of group (a 'group' is an analysis of identical markers).

☒ All plots are contour plots with outliers or pseudocolor plots.

☒ A numerical value for number of cells or percentage (with statistics) is provided.

Methodology

Sample preparation	Mice were anaesthetized with ketamine (100 mg/kg) and xylazine (10 mg/kg) in saline by i.p. injection and then transcardially perfused with ice-cold PBS. The lymph nodes were then dissected and gently pressed through 70-μm nylon mesh cell strainers with a sterile plastic plunger to obtain a single-cell suspension. The brain was digested with collagenase IV (0.05%;

Sigma Aldrich) and DNAse I (10 µg/mL; Roche) for 60 min at 37 °C before being strained. Then, tissue masses were homogenized by gently pressing them through tissue sieves. Cells were then centrifuged at 300g for 5 min. Mononuclear cells were prepared by 37 %/70 % Percoll (GE Healthcare, Princeton, NJ, USA) centrifugation at 300g for 30 min at 25 °C. The cell pellets were washed with PBS, resuspended in ice-cold PBS and were stained with antibody cocktails.
To FACS sort meningeal lymphatic endothelial cells (LECs), mice were anaesthetized with ketamine (100 mg/kg) and xylazine (10 mg/kg) in saline by i.p. injection and then transcardially perfused with ice-cold PBS. Meninges were carefully removed, and then digested for 15 min at 37 °C with 0.05% collagenase VIII (Sigma Aldrich) and 10 µg/mL of DNAse I (Roch) in DMEM (Gibco) with 2% FBS (Atlas Biologicals), 1% l-glutamine (Gibco), 1% penicillin/streptomycin (Gibco), 1% sodium pyruvate (Gibco), 1% nonessential amino acid (Gibco) and 1.5% HEPES (Gibco). The digested meninges were gently pressed with sterile plastic plunger and then single-cell suspensions were obtained after filtration through a 70-µm nylon-mesh cell.

Instrument

BD LSRFortessa (BD Biosciencess) was ued for Flow cytometry assays. FACSAria Sorp (BD Biosciencess) was ued for Flow cytometry sorting.

Software

Flowjo.10.4 software was used to analyze data.

Cell population abundance

The detailed data were provided in the figure 1 n and Extended Data figure 6.

Gating strategy

Singlets were gated along the diagonal when forward scatter height (FSC-H) versus forward scatter area (FSC-A) was plotted. Cells negative for FVD506 were gated as viable cells. Microglia was gated as CD45intCD11b+. Neutrophil was gated as CD45hi CD11b+Ly6G+. Macrophage was gated as CD45hi CD11b+Ly6G-F4/80+. Monocyte was gated as CD45hi CD11b+Ly6G-F4/80-Ly6C+. B cell was gated as CD45hi CD19+ or CD45hi B220+MHCII+. NK cell was gated as CD45hiCD19-NK1.1+. CD4+T cell was gated as CD45hi CD19-NK1.1-CD4+. CD8+T cell was gated as CD45hi CD19-NK1.1-CD8+. DCs were gated as CD45hi CD11c+ MHCII+. The meningeal LECs were then gated as DAPI−CD45−CD31+PDPN+; The detailed data were provided in the Extended Data figure 6 and Extended Data figure 5g.

☒ Tick this box to confirm that a figure exemplifying the gating strategy is provided in the Supplementary Information.